Measurement of the fusion barrier distribution for the $^{86}Kr + ^{208}Pb$ reaction

Sifiso Senzo Ntshangase

Thesis submitted in partial fulfillment of the requirements
for the degree of Master of Science
in the Department of Physics and Engineering
University of Zululand
November 2005

MEASUREMENT OF THE FUSION BARRIER DISTRIBUTION FOR THE $^{86}Kr + ^{208}Pb$ REACTION

Abstract

The main object of this work is to investigate a method of determining the total capture cross-section without passing through separate measurements of quasi-fission, fusion-fission and evaporation residue, using the fact that the sum of the flux in the various final channels is equal to the total incident flux. Thus capture is complementary to the flux reflected from the barrier. Here we present an experiment performed at the cyclotron facility at iThemba LABS to determine the fusion barrier distribution for the $^{86}Kr + ^{208}Pb$ reaction using the method of measuring quasi-elastic scattering proposed by Dr. N. Rowley.

ACKNOWLEDGEMENTS

I wish to express my sincere gratitude to the following people for making the realization of this work possible:

- My research supervisor Dr. R.A. Bark for the guidance, active participation, continous support and for the undying patience he gave me during his supervision of this investigation;

- Dr. J.J. Lawrie for allowing me to pursue this research in the Physics group and for the active participation during the measurement;

- Prof. O.M. Ndwandwe my university supervisor at the Physics and Engineering Department of the university of Zululand for his interest and support;

- Dr. N. Rowley, for his willingness to guide me and for assisting with the intepretation of the data although he was far away. I owe you so much that it is difficult to express my sincere word of gratitude in any other way-*kwanda kwaliwa ngabathakathi Mnumzane*;

- Dr. S.V. Förtsch, Dr. S.M. Mullins, Dr. F.D. Smit, Dr. E.A. Gueorguieva-Lawrie, Dr. R. Nevelling and Dr. H. Fujita for active participation in the experiment and for the daily assistance you gave me;

- Prof. J.F. Sharphey-Schafer for the love he gave to all the students while he was a director at iThemba LABS and for reading this thesis;

- Lastly, I must thank my family for their love and support. Their encouragement over the years made tough times easer; without them I could never have made it this far.

CONTENTS

LIST OF FIGURES

LIST OF TABLES

CHAPTER 1 INTRODUCTION

1.1 HISTORICAL EVOLUTION

The major part of this work was motivated by the prediction concerning the possible existence of an "island of stability" beyond the presently known mass region of particle-stable nuclei. Extrapolations of the nuclear shell model towards larger masses indicate that the next major shell effect is predicted to be particularly strong for nuclei with N=184 and Z=114 [Sob94, Smo94, Möl94]. Figure 1.1 illustrates the closed shells and the region of superheavy elements (SHE) as the nuclear models predict, with the proton number on the vertical, and neutron number on the horizontal axis.

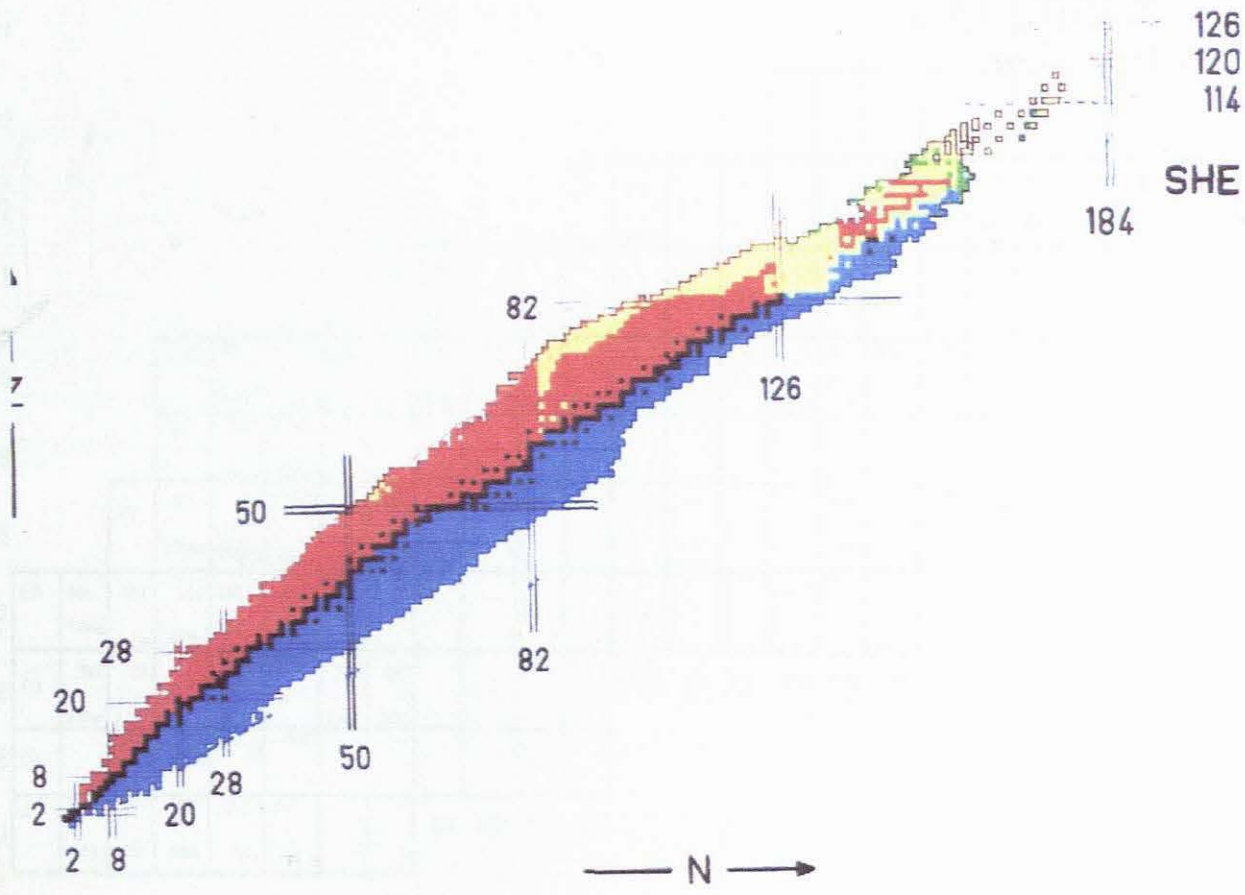

Figure 1-1: The double closed shells as predicted by the nuclear models, from [Ter01].

Experiments to search for the doubly magic closed shell nucleus have been negative so far. Heavy-ion reactions have been used in attempts to produce these superheavy elements. In these reactions, two nuclei, one in a heavy-ion beam, the other in a target, are fused together to create a compound nucleus [Ste94, Bud81, Hui81]. Using this method elements as heavy a $Z=116$ have been synthesized [Hof01]. As a result of the synthesis of these heavier elements, the upper end of the nuclear chart today is shown in figure 1.2.

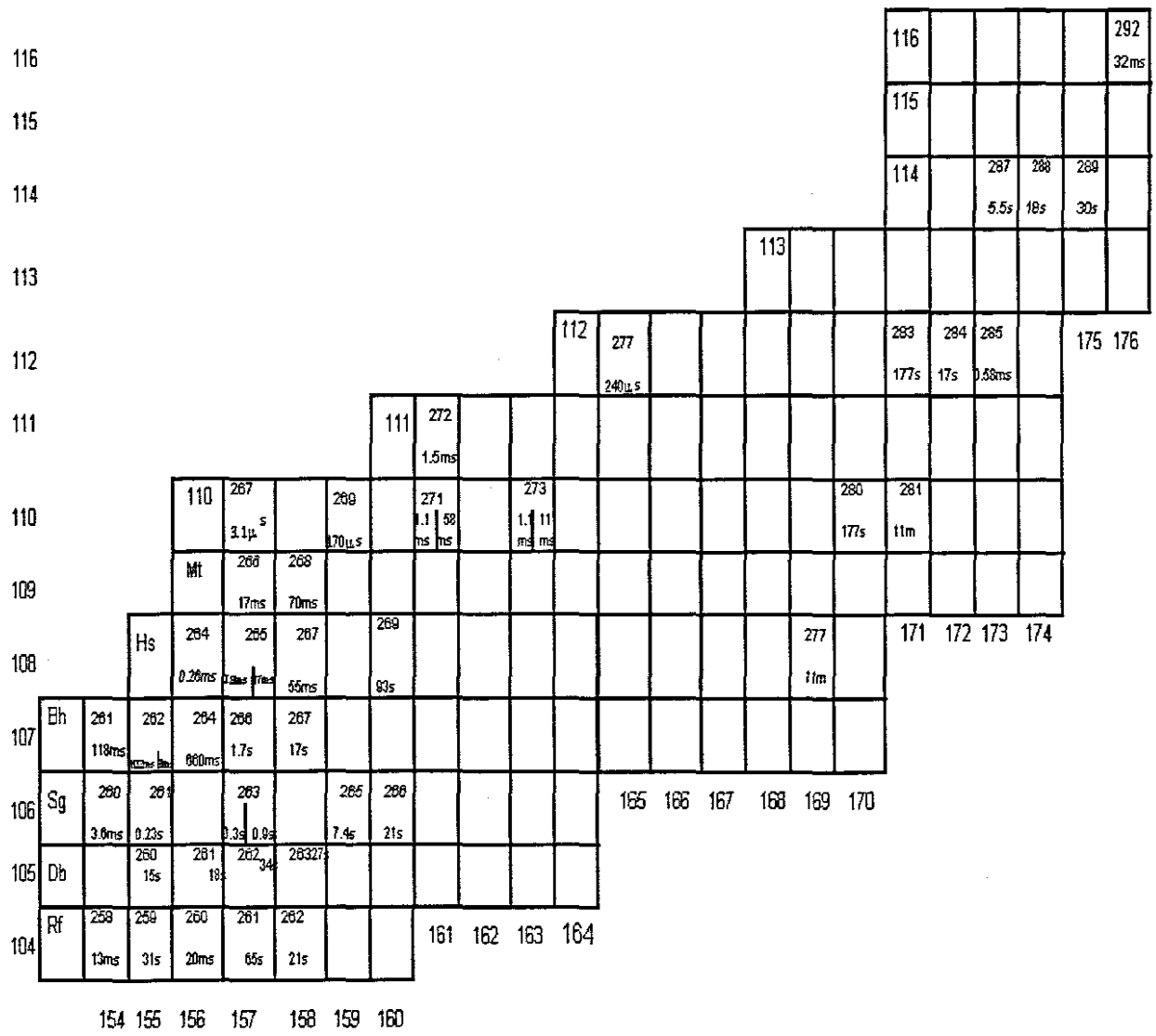

Figure 1-2: The upper end of the nuclear chart with the known isotopes and the experimental half-lives of the transactinides as it appears today, [Hof00].

The trouble with this approach is that the collision between the ions leaves the resulting compound nucleus in a highly excited state, therefore it easily separates into two more or less equal fragments immediately (fission). The stabilizing effect of nucleon shells also decreases rapidly with increasing excitation energy [Ele94]. The synthesis of the superheavy elements has motivated scientists to heavily embark on investigations of the study of nuclear reactions. Therefore in this investigation the quasielastic cross-section for $^{86}Kr + ^{208}Pb$ has been measured as a primary step to study the complicated fusion cross-section for superheavy elements.

1.2 OVERVIEW

Reactions between heavy nuclei with $Z_t Z_p < 1500$ (where Z_t and Z_p are the atomic numbers of the target and the projectile nuclei) are rather well understood [Ike00]. In a very simple system like the double closed-shell system such as $^{40}Ca + ^{40}Ca$ the reaction is mediated by the presence of a single Coulomb barrier [Ada04]. As a result, flux which does not penetrate the single barrier is elastically scattered. Flux that does penetrate the barrier forms a nucleus that quickly loses memory of it formation, (the compound nucleus). This compound nucleus may form a stable long-lived nucleus after particle evaporation, (evaporation-residue) or else it may undergo fission if the combined atomic number, Z is sufficiently large.

However, reaction systems that may result in the production of superheavy elements have $Z_t Z_p > 1500$ [Mos81]. In these reactions the processes resulting from the collision of the two very heavy nuclei are much more complex. This is due to the huge Coulomb barrier created because of the presence of the electrostatic force existing between the charge of the projectile and the target.

Measurements show a diminishing production cross-section which are in order of picobarns for the heavy system. Figure 1.3 illustrates some of the measured cross-sections for the production of superheavies for energies above the barrier or high

excitation energies (hot fusion) and energies below the barrier or low excitation energies (cold fusion).

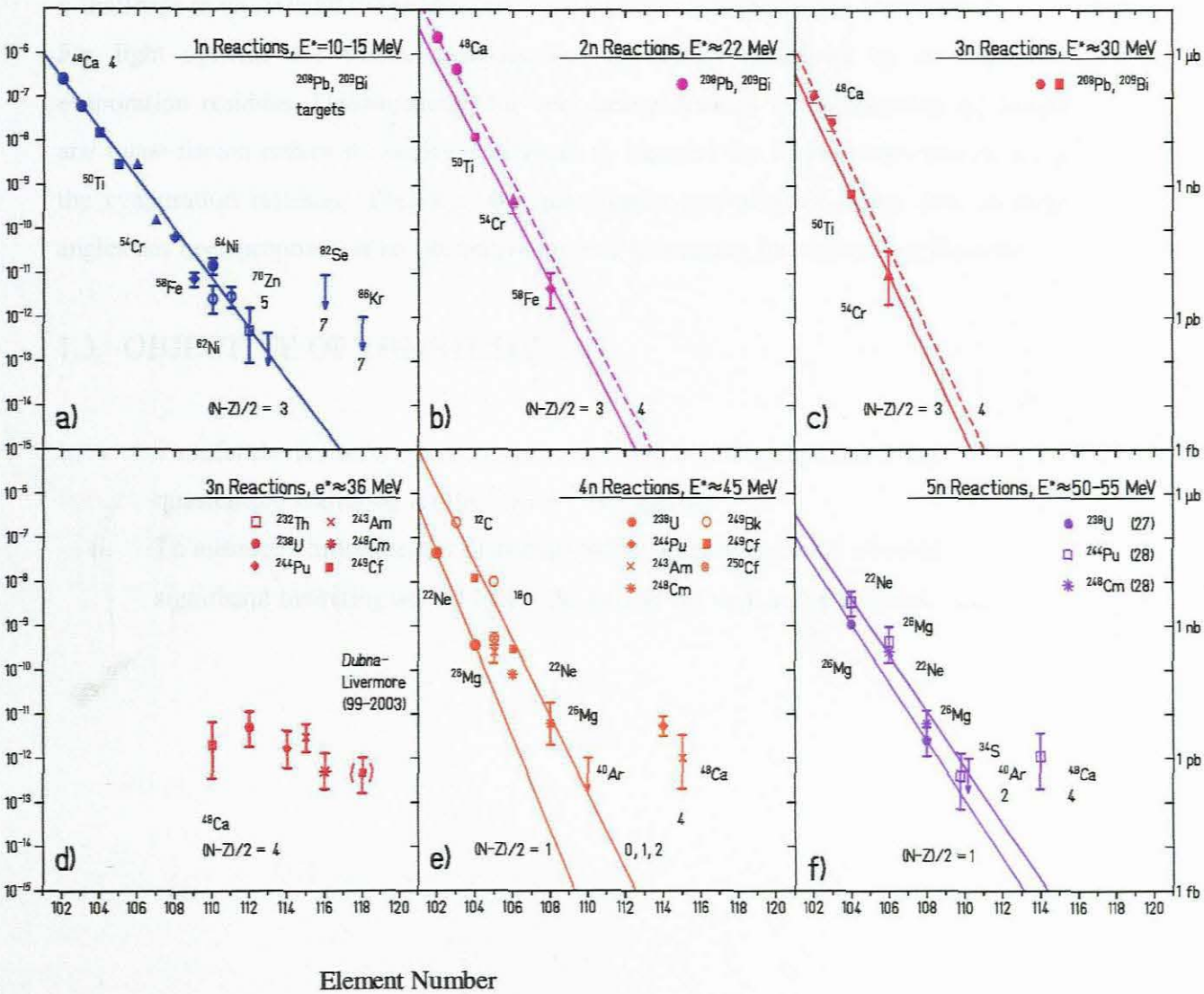

Figure 1-3: Measured cross-section for superheavy elements in hot and cold fusion reactions, from [Hof97].

The $^{86}Kr + ^{208}Pb$ reaction that we are studying in this measurement, is one of the heavy systems which has been used in an attempt to make a superheavy element, $Z = 118$. It was unsuccessful because of the very small production cross-sections. Therefore it is still a challenge to understand the production cross-section of these superheavy elements.

For light systems the fusion cross-sections are easily measured by detecting the evaporation residues. Unfortunately, for very heavy systems the domination of fission and quasi-fission makes it extremely difficult to measure the fusion cross-section using the evaporation residues. Therefore the quasielastic scattering of heavy ions at large angles has been proposed as an alternative method to measure fusion barriers [Den00].

1.3 OBJECTIVE OF THE STUDY

i. To infer the fusion cross-section as a function of energy by measuring quasielastic scattering for the $^{86}Kr + ^{208}Pb$ system.

ii. To measure "fusion barrier distributions" in order to examine whether significant tunneling occurs below the barrier for very heavy systems.

CHAPTER 2 THEORY

2.1 HEAVY ION REACTIONS

A nuclear reaction is a process whereby a nucleus is transformed from one species to another. These reactions involve the collision of an accelerated projectile with a target nucleus. In these reactions the initial system is transformed into the final system, consisting of the products of the reaction. Symbolically [Fes92];

$a + X \rightarrow Y + b$

where a is the accelerated projectile, X is the target (usually stationary in the laboratory), Y and b are the reaction products. Usually, Y is the heavy product and b are light particles that can be detected e.g. α-particles, γ-rays, neutrons etc. [Kra88]. According to the classical picture, the projectile can induce various kinds of reactions depending on the impact parameter or the corresponding angular momentum.

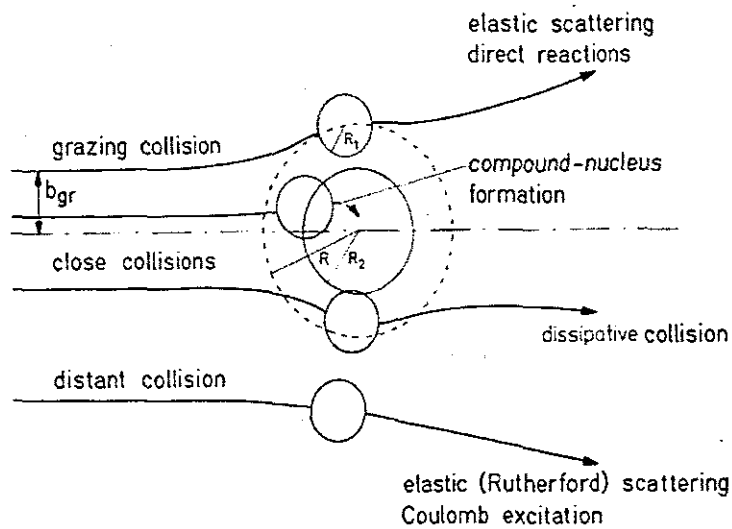

Figure 2-1: Distant, grazing and close collisions in the classical picture of heavy ion collisions, from [Gle75].

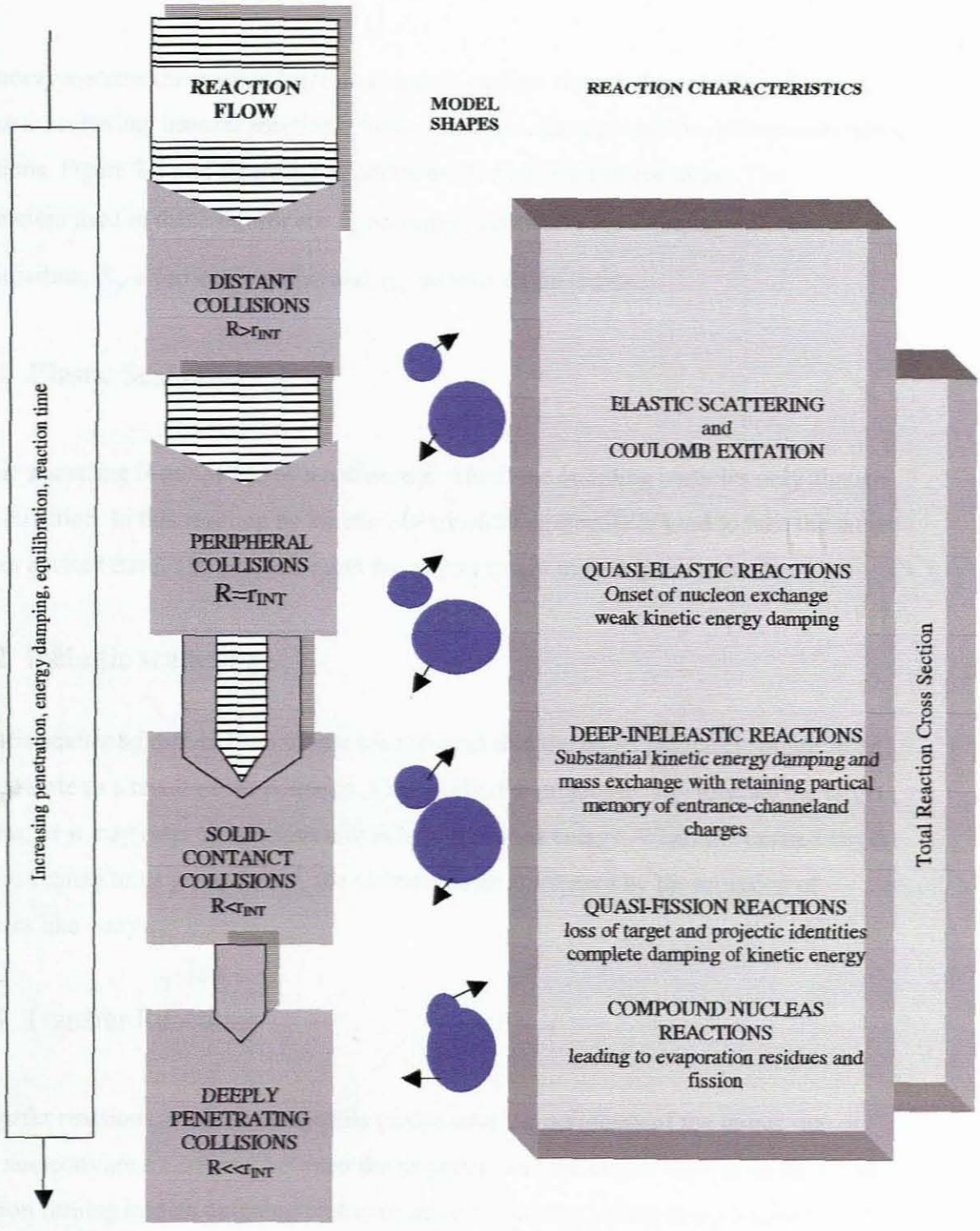

Figure 2-2: Schematic classification of heavy-ion reactions, from [Sch84].

For heavy systems the various reaction channels can be referred to as elastic scattering, inelastic scattering, transfer reactions, fusion reactions, fission reactions and quasi-fission reactions. Figure 2.1 and figure 2.2 illustrate the various nuclear reactions. The parameters used in these figures are b_{gr} an impact parameter for a grazing collision, R_t a target radius, R_p a projectile radius and r_{int} an interaction radius.

2.1.1 Elastic Scattering

Elastic scattering is defined to be a collision in which the colliding particles only change their direction. In this reaction no kinetic energy of the projectile is used to take the target into an excited state. The projectile and the target remain in their ground states.

2.1.2 Inelastic scattering

Inelastic scattering differs from elastic scattering in that the target nucleus is raised to an excited state as a result of the collision. Classically, the projectile only touches the target nucleus, or it may enter the nucleus and exit at a reduced energy. When the excited target nucleus returns to its ground state, the excess energy is released by the emission of particles like γ-rays.

2.1.3 Transfer Reactions

In transfer reactions, when the projectile passes over the periphery of the target, one or more nucleons are transferred between the projectile and the target, such as an incoming deuteron turning into an outgoing proton or neutron, thereby adding some nucleons to the target X to form a nucleus, Y.

2.1.4 Quasielastic scattering

In quasielastic scattering the projectile loses a moderate amount of energy and exchanges a few nucleons with the target nucleus. Quasielastic reactions are assumed to correspond to collisions in which the surfaces of the two ions have just been in a grazing contact. However, in this study, quasielastic will refer to the sum of all the elastic scattering, inelastic scattering and transfer reactions.

2.1.5 Deep inelastic

This reaction entails substantial damping of kinetic energy and mass exchange. The larger fragments are highly deformed and excited while retaining partial memory of "target" and "projectile" masses and charges [Sch91a]. This process takes place at energies above the Coulomb barrier.

2.2 THE COULOMB BARRIER

The most familiar barrier to penetrate is the Coulomb barrier, present because of the electrostatic repulsion between the positively charged target nucleus and the positively charged projectile. As the two partners are of comparable mass, the system is more easily described in terms of their relative motion in the center-of-mass system. Assuming the standard laboratory situation of a fixed target, which is bombarded with a beam of projectile nuclei, the relation between the kinetic energy E_{lab} as measured in the laboratory system and the kinetic energy E_{cm} in the center-of-mass system is given by

$$E_{cm} = \frac{A_t}{A_t + A_p} E_{lab} \qquad 2.1$$

where A_p and A_t represent the mass number of the projectile and target nuclei, respectively. Electron masses and differences in binding energy per nucleon may be ignored as a good approximation. The motion of the center-of-mass is fully determined by the kinematics of the reaction and can be calculated from the bombarding energy and

the nuclear masses. Quantum mechanically the nuclear binary system may be represented by the wave function $\Psi(r)$. Using the center-of-mass parameterization, the combined effect of the Coulomb and the nuclear force between the two nuclei can be expressed as the interaction potential. These have been illustrated in figure 2.3.

$$V(r) = V_C(r) + V_n(r) \qquad 2.2$$

where V_C are the Coulomb and V_n the nuclear potential. The motion of the binary system is then described by the Schrödinger equation.

$$\left[-\frac{\hbar^2 d^2}{2\mu dr^2} + \frac{l(l+1)\hbar^2}{2\mu r^2} + V(r) - E \right] \Psi(r) = 0 \qquad 2.3$$

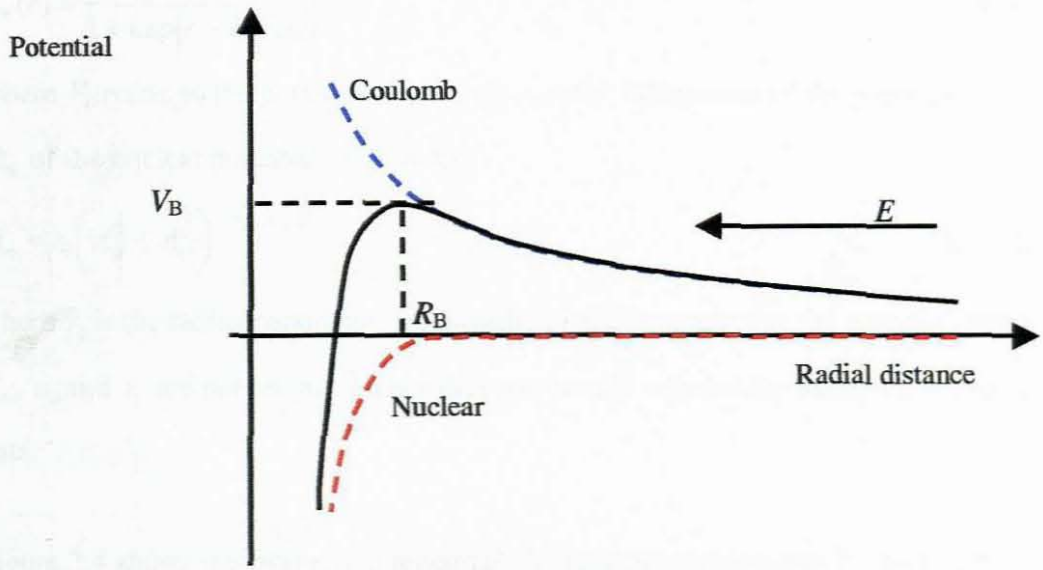

Figure 2-3: The illustration of the potentials that form a barrier between the participating nuclei in a nuclear reaction.

At large distances r, the Coulomb potential V_C has the form of the electrostatic potential for two point-charges. At close approach, when the charge distributions overlap, the point-charge has to be modified. This is often achived by replacing one of the point charges with a homogeneously charged sphere of radius R_C, so that

$$V_C(r) = Z_p Z_t e^2 \begin{cases} 1/r & for \quad r > R_C \\ \left(\frac{3}{2} - \frac{r^2}{2R_C^2}\right) \Big/ R_C & for \quad r \le R_C \end{cases} \qquad 2.4$$

Since during the collision there occurs a large number of interactions between the projectile and the target nucleons, it has not been possible to determine the nuclear potential V_n from the known two-body forces between nucleons. It is therefore common practice to make a simple parameterization, approximating the nuclear potential with a function which resembles the nuclear mass distribution. This results in the Woods-Saxon potential

$$V_n(r) = \frac{-V_0}{1 + \exp(r - R_n/a_0)} \qquad 2.5$$

where V_0 refers to the potential depth and a_0 is the diffuseness of the potential. The radius R_n of the nuclear potential is given by;

$$R_n = r_0\left(A_p^{\frac{1}{3}} + A_t^{\frac{1}{3}}\right) \qquad 2.6$$

where r_0 is the radius parameter. It is worthwhile to mention that the potential parameters V_0, a_0 and r_0 are not unique. Hence they are usually adjusted by fitting experimental data.

Figure 2.4 shows the interaction potential $V(r)$ and its components V_C and V_n for ^{144}Sm + ^{16}O. The competition between the electrostatic and the nuclear forces gives rise to a potential barrier at a distance R_0. At its vertex the shape of the barrier may be approximated by an inverted parabola [Tho59]. Since this is a good approximation at energies close to the barrier height, the exact potential is often replaced by this function. When two nuclei overcome the Coulomb barrier and reach the potential pocket they can form a composite system and fuse.

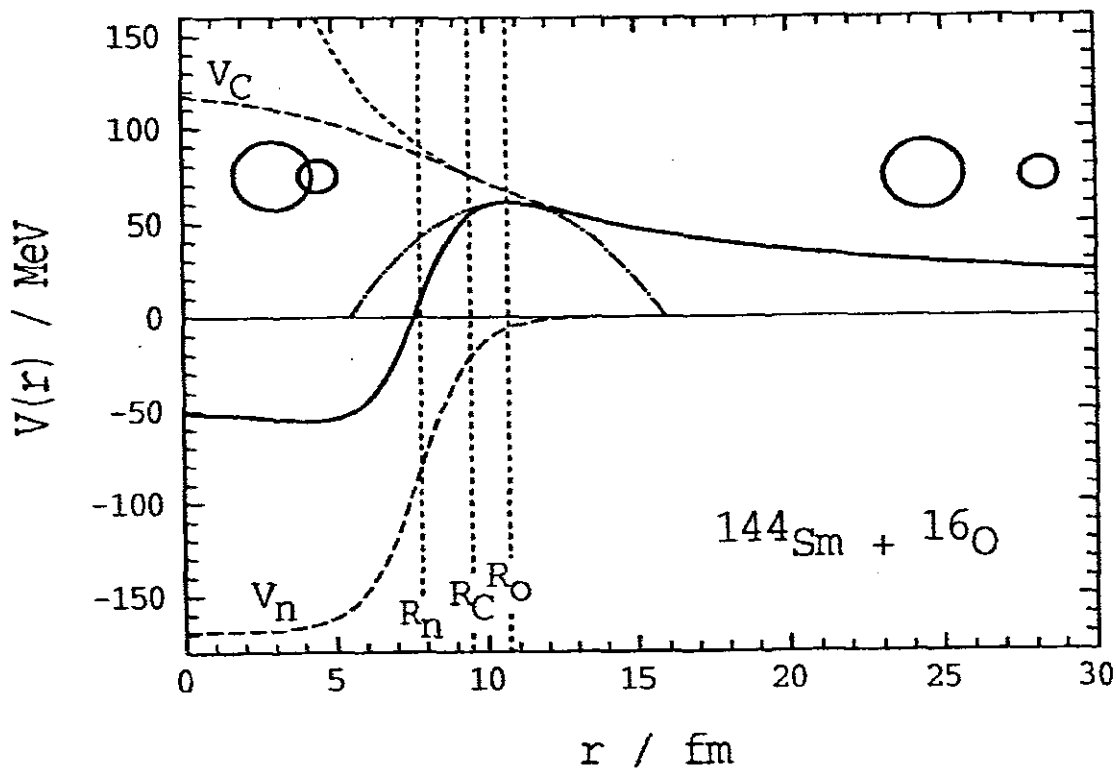

Figure 2-4: The interaction potential $V(r)$ (solid) for $^{16}O+^{144}Sm$ in a head-on collision. The potential is of the Coulomb potential V_C and the nuclear potential V_n (long-dashed curves). At its vertex, the potential barrier may be approximated with an inverted parabola (dot-dashed). The point charge approximation of the Coulomb potential is shown as short-dashed curve. The radial distances R_n, R_C and R_0 are defined in the text, from [Tho59].

In the opposite direction, a single nucleus can overcome the analogous but different fission barrier to scission into two unbound fragments in the fission process [Hil92]. The motion over the barrier can couple to internal degrees of freedom of the nuclei, which include excitations and mass transfer.

2.3 NUCLEAR FUSION

Fusion may be defined as an amalgamation of the projectile and the target to form a compound nucleus such that the charge and mass of the compound nucleus formed can be described by equation 2.7.

$$(A_c, Z_c) = (A_1 + A_2, Z_1 + Z_2) \qquad 2.7$$

In this equation the right hand side stands for a state of the system, which is completely characterized by its total mass, charge, energy, and angular momentum and has reached equilibrium with respect to all other internal degrees of freedom [Bas80].

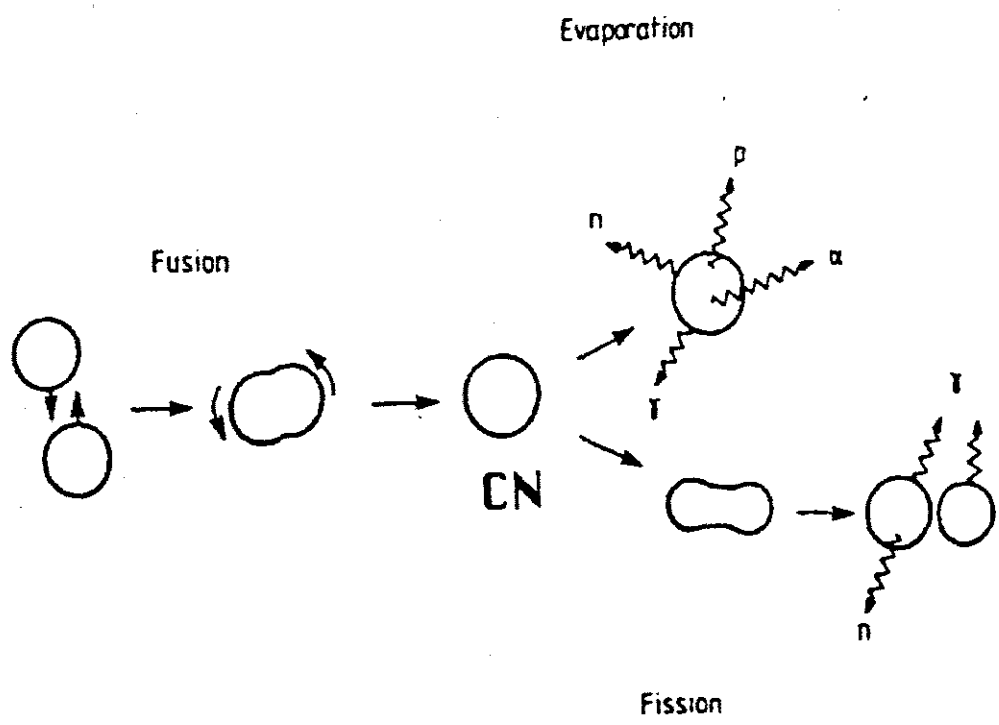

Figure 2-5: The formation and the decay of a compound nucleus, from [Tim96].

In general, the compound nucleus is initially in a highly excited state due to the excitation energy. This compound nucleus decays via particle emission [Wei37] or fission [Boh39] and γ-ray emission as illustrated in figure 2.5. In light nuclei, with $Z \leq 70$, the

probability of fission is typically so small that all decays proceed via particle emission [Boh39]. This particle emission is often referred to as particle evaporation. The evaporated particles are predominantly neutrons, but also protons and α-particles. This decay mode results in a nucleus, dubbed the evaporation residue.

2.3.1 Fission

Fission is another way that the compound nucleus can decay. When nuclear fission occurs, the nucleus splits principally into two smaller fragments. These fragments, or fission products, are about equal to half the original mass. Two or three neutrons are also emitted, as illustrated in figure 2.6. The sum of the masses of these fragments is less than the original mass. Fission can occur when a nucleus of a heavy atom captures a neutron, or it can happen spontaneously in unstable nuclei. In the decay of heavier compound nuclei with $Z_c \geq 70$, fission competes with particle evaporation and dominates for very large atomic number, Z_c even at energies below the barrier height [Lie82, Pla84].

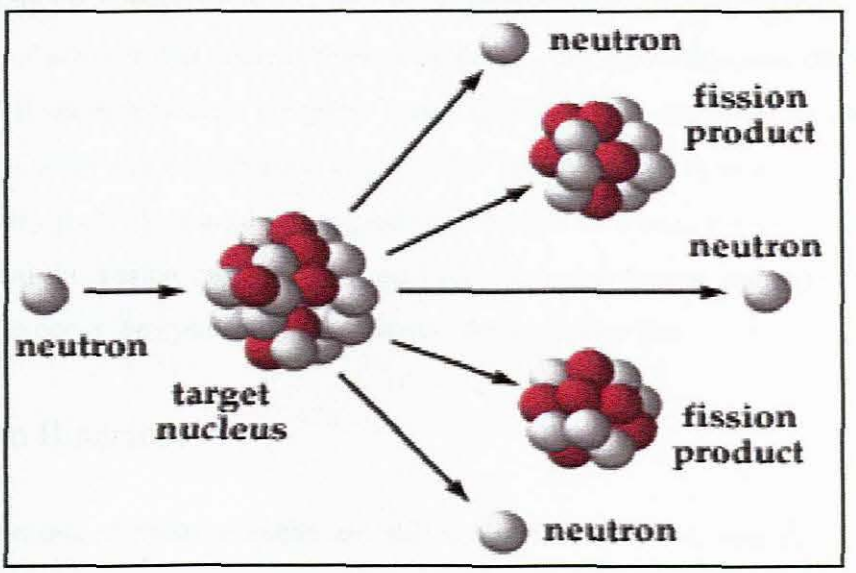

Figure 2-6: The illustration of nuclear fission process, from [www1].

Furthermore, because of the large overlap, deep-inelastic reactions with a massive loss of energy and an exchange of many nucleons occur for heavy systems, resulting in reaction products that may be similar to fission fragments. While deep-inelastic reactions have to be rejected, both the evaporation residue cross-section and the fission cross-section have to be measured in order to establish the fusion cross-section.

2.3.2 Quasi fission

Fusion does not occur easily for a heavy projectile and target. The result of the process of rapid separation into two fragments before the compound nucleus is formed is called quasi fission. For very heavy compound nuclei, where fission is important, it is not necessarily straightforward to establish experimentally that an equilibrated compound nucleus has been formed. The fission barrier may be located inside the fusion barrier, so that a quasi-fission process of the unequilibrated composite system is observed in addition to fission after compound nucleus formation [Lem93, Bac85]. Quasi fission is characterized by the emergence of fission-like fragments which do not originate from the fission decay of a compound nucleus formed by fusion, but rather from the fission break up of a short lived intermediate complex. Quasi fission can be described as the second class of fusion, since the equilibration occurred for energy charge symmetry, but not for mass asymmetry [Lef76]. It has been argued [Hid95] that in investigations of the fusion barrier problem the fission cross-section must include quasi-fission reactions, since for quasi-fission to occur the system has to overcome the fusion barrier.

2.3.3 Fusion Hindrance

Fusion mechanisms of massive nuclei are still not well understood, though it is known that fusion is hindered in systems with $Z_t Z_p \geq 1500$ [Bas77]. These systems do not fuse even with incident energies being well above the expected barrier. The so-called "extra-push" energy is necessary in addition to the barrier height. This could be interpreted as a friction force acting between two colliding nuclei in the approaching phase as well as by a dissipation of the collective motion that leads to the formation of the compound nucleus

[Oga75]. The difference in barrier height, dubbed 'extra-push', can be used to explain this phenomenon of apparent fusion hindrance. The extra-push increases with the product of $Z_t Z_p$. It is therefore roughly a function of the size of the system. With increasing size the number of degrees of freedom of the system rises dramatically. In particular the number of transfer channels increases [Rei94]. Thus fusion may be preceded by the massive exchange of nucleons. This would have several consequences. Firstly, the potential energy is affected because of the redistribution of nucleons between projectile and target nucleus [Mos80], e.g. more symmetric charge distributions result in higher fusion barriers. Secondly, the potential energy of the system is also modified by the presence of nuclear matter between the reactants, which is often referred as a neck-formation. Thirdly, the system has to dissipate kinetic energy to open the various reaction channels. The observation of fusion hindrance has been interpreted as a signature of these effects and models have been developed which treat fusion as a multi-dimensional potential energy surface as a function of distance, mass-asymmetry, neck formation and energy dissipation [Swi81, Blo86].

2.3.4 Barrier penetration

At a bombarding energy below the Coulomb barrier, fusion is classically forbidden [Bas80], but can nevertheless occur due to quantum-mechanical barrier penetration [Jor86]. The probability of penetration can be described with a transmission coefficient, $T(E)$ and a reflection coefficient, $R(E)$. The transmission coefficient measures the penetration probability and the reflection coefficient measures the probability that the barrier reflects the flux. Because the incident flux is either reflected or transmitted, the conservation of flux can be expressed as;

$$T(E)+R(E)=1 \qquad 2.8$$

The transmission coefficient $T(E)$ through a one-dimensional barrier can be calculated using the Wentezel-Krammer-Brillouin method [Kem36, Fro65], in which case it is given by [Hil53].

$$T(E) = \left(1 + \exp[2K(E)]\right)^{-1} \qquad 2.9$$

with $K(E)$ is given by

$$K(E) = \pm \int_{r_i}^{r_0} \sqrt{\frac{2m}{\hbar^2}|V(r) - E|}\,dr \qquad 2.10$$

where r_i and r_0 refer to the inner and outer points of the barrier.

The minus and plus signs in front of the integral in equation 2.10 correspond to energies E above the barrier or below B_0, respectively. A barrier shape which is of interest because of its mathematical simplicity is that of an inverted parabola [Won73]. It may be expressed as

$$V(r) = B_0 - \frac{m\omega_0^2}{2}(r - R_0)^2 \qquad 2.11$$

where R_0 is the barrier position and ω_0 is the eigen-frequency of the harmonic oscillator potential $V(r)$. The transmission coefficient for this special case is given by equation 2.12 [Hil53].

$$T(E) = \left(1 + \exp\left[\frac{2\pi}{\hbar\omega_0}(B_0 - E)\right]\right)^{-1} \qquad 2.12$$

When the energy equals the barrier height B_0, the transmission coefficient is 0.5, whereas at energies below B_0 it can still be considerably larger than zero.

2.3.5 Fusion excitation functions

By extending the theoretical description to three spatial dimensions it has to be taken into account that the interaction potential $V_l(r)$ depends on the orbital angular momentum $l\hbar$ with

$$V_l(r) = V(r) + V_{cent}(r, l) \qquad 2.13$$

Where $V(r)$ is the sum of the Coulomb ($V_C(r)$) and nuclear potential ($V_n(r)$) and $V_{cent}(r, l)$ is the centrifugal term with

$$V_{cent}(r,l) = \frac{\hbar^2}{2\mu r^2} l(l+1) \qquad 2.14$$

where l and μ are the relative angular momentum and the reduced mass of the system respectively. As illustrated in the figure 2.7, the centrifugal potential increases the barrier height and shifts the barrier position to smaller radii with increasing orbital angular momentum. For large angular momentum (l) it eventually fills in the attractive pocket and thus restricts fusion to small angular momenta. For an angular momentum dependent potential the transmission function becomes also angular momentum dependent with $T(E) \equiv T_l(E)$ and for each l the fusion probability can be expressed as the differential cross section

$$\sigma_l^{fus}(E) = \pi\lambda\!\!\!^{-2}(2l+1)T_l(E) \qquad 2.15$$

where $\lambda\!\!\!^{-} = \frac{\hbar}{p}$ is the reduced de Broglie wavelength associated with the relative motion.

By summing over all angular momenta, the total fusion cross-section is obtained as

$$\sigma^{fus}(E) = \sum_{l=0}^{\infty} \pi\lambda\!\!\!^{-2}(2l+1)T_l(E) \qquad 2.16$$

This energy dependent function is generally referred to as the fusion excitation function [Rho84]. The transmission coefficient for partial wave l at energy E can be expressed as

$$T_l(E) = \left(1+\exp\left[\left(\frac{2\pi}{\hbar\omega}\right)\left(B - E + \frac{\hbar^2 l(l+1)}{2\mu R^2}\right)\right]\right)^{-1} \qquad 2.17$$

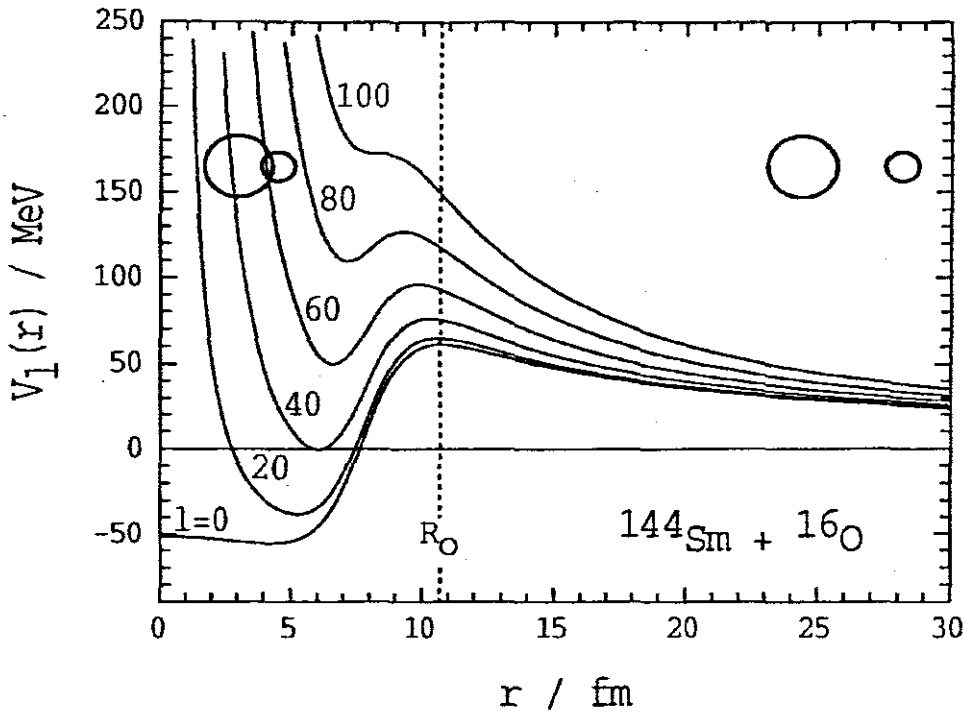

Figure 2-7: The interaction potential $V_l(r)$ for $^{144}Sm+^{16}O$ as a function of angular momentum l. R_0 indicates the position of the barrier for $l = 0$, from [Rho84].

The relationship between the incident flux and the scattered flux can be expressed in a form of a matrix named a scattering matrix [Sch68]. The scattering matrix relates the final and the initial states of the target. It may be defined as unitary matrix connecting the asymptotic particle states [Sch68]. The Scattering matrix is closely related to the transition probability amplitude and the cross section of various interactions. The transmission coefficient can be written in terms of scattering matrix as;

$$T_l(E) = 1 - |S_l|^2 \qquad 2.18$$

where S_l is the scattering matrix. Substituting equation 2.18 in equation 2.16 it can be shown that the total fusion cross-section [Hod83] can be given by

$$\sigma^{fus}(E) = \sum_{l=0}^{\infty} \pi\lambda\!\!\!^{-2}(2l+1)\left(1 - |S_l|^2\right) \qquad 2.19$$

2.4 SINGLE BARRIER MODEL

At high energies, heavy-ion fusion cross sections σ^{fus} behave in a rather classical manner. Fusion seems to occur if the energy E is sufficient for the ions to pass over the potential barrier between them. Therefore, classically in the one-dimension barrier penetration model, the fusion cross section σ^{fus} at energy E is given by a summation over all partial waves up to $l = l_g$ [Row90], where l_g is the grazing angular momentum. If the grazing angular momentum is defined to be that for which the total barrier height is equal to E then

$$E = B + \frac{l_g(l_g+1)}{2\mu R^2} \qquad 2.20$$

where B is the barrier height, and classically all the partial waves up to l_g will fuse. Approximating the summation in equation 2.16 as an integral, gives

$$\sigma^{fus} \approx \frac{\pi\hbar^2}{2\mu E}\int_0^{\infty}(2l+1)T_l\,dl = \frac{\pi\hbar^2}{2\mu E}\int_0^{l_g}(2l+1)dl$$

$$= \frac{\pi\hbar^2}{2\mu E} l_g(l_g+1)$$

$$= \pi R^2\left(1-\frac{B}{E}\right) \qquad 2.21$$

where the parameter R, E and B are the position of the barrier, beam energy and barrier height respectively. It is well known that in the absence of coupling the fusion cross-section is described by the classical expression in equation 2.21 [Das98].

Classically, for $E < B$, the product $\sigma E = 0$ while for $E \geq B$, $E\sigma = \pi R^2(E-B)$, from which we obtain

$\frac{d(\sigma E)}{dE} = 0$ for $E < B$ and $\frac{d(E\sigma)}{dE} = \pi R^2$ for $E \geq B$, thus

$$\frac{1}{\pi R^2}\frac{d^2(E\sigma)}{dE^2} = \delta(E-B) \qquad 2.22$$

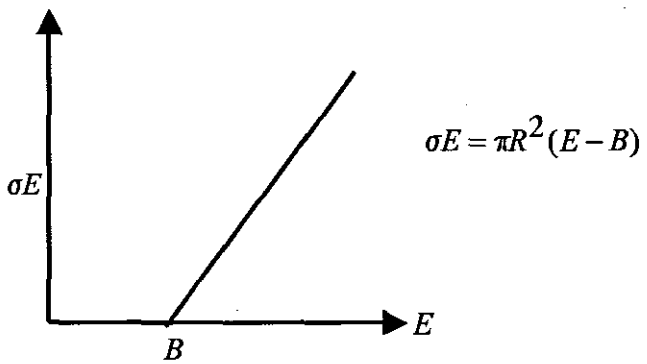

Figure 2-8: The plot of σE as a function of energy E, The plot clearly shows that classically, fusion cannot occur at energies below the barrier B.

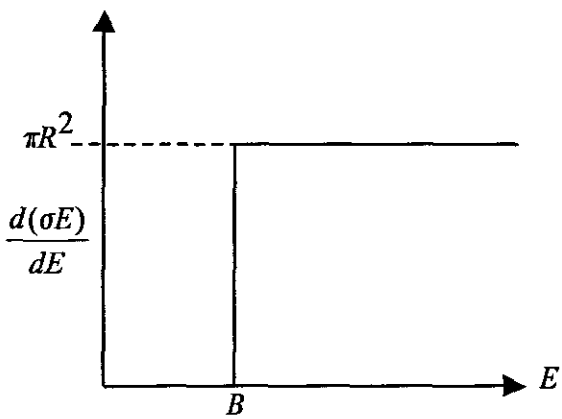

Figure 2-9: The first derivative of the plot is a constant, πR^2 above the barrier.

The second derivative of equation 2.21 results in a δ-function, which represents the barrier position and height as shown in figure 2.10.

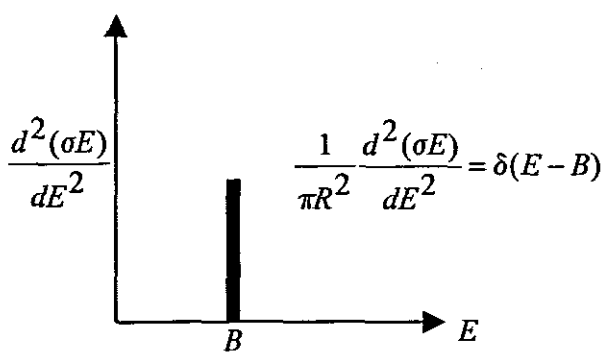

Figure 2-10: The second derivative showing the barrier position.

2.5 EXPERIMENTAL EVIDENCE FOR DISTRIBUTION OF BARRIERS

In the fusion of heavy nuclei, there may be more than one fusion barrier or a distribution of barriers, to overcome. For example, in the case of statically deformed nuclei, experimental data show that different physical configurations of the colliding nuclei corresponds different fusion barrier energies. This is illustrated in figure 2.11, which shows the data for ^{16}O + $^{144,148,150,152,154}Sm$. In these isotopes of ^{A}Sm, the deformation increases with the neutron number. A distribution of barriers can be understood classically in the case of deformed nuclei, where different orientations of the deformed nuclei with respect to the incident projectile result in fusion barriers at different radii and thus energy [Lei95]. Compared with the spherical problem, the Coulomb barrier is low when the projectile approaches the pole of a deformed Sm target and is higher when it approaches the equator. This has been seen in the fusion of ^{A}Sm with ^{16}O; the fusion cross-section for ^{144}Sm decreases rapidily than the other Sm isotopes. Taking into account all the possible orientations produces a continous distribution of barrier heights, some of which are lower and some are higher than the single barrier. The lower barrier gives larger than expected cross-sections at energies below the original barrier. Therefore it is now well established that in the fusion of heavy nuclei, there is not a single barrier, but a distribution of fusion barriers [Das83].

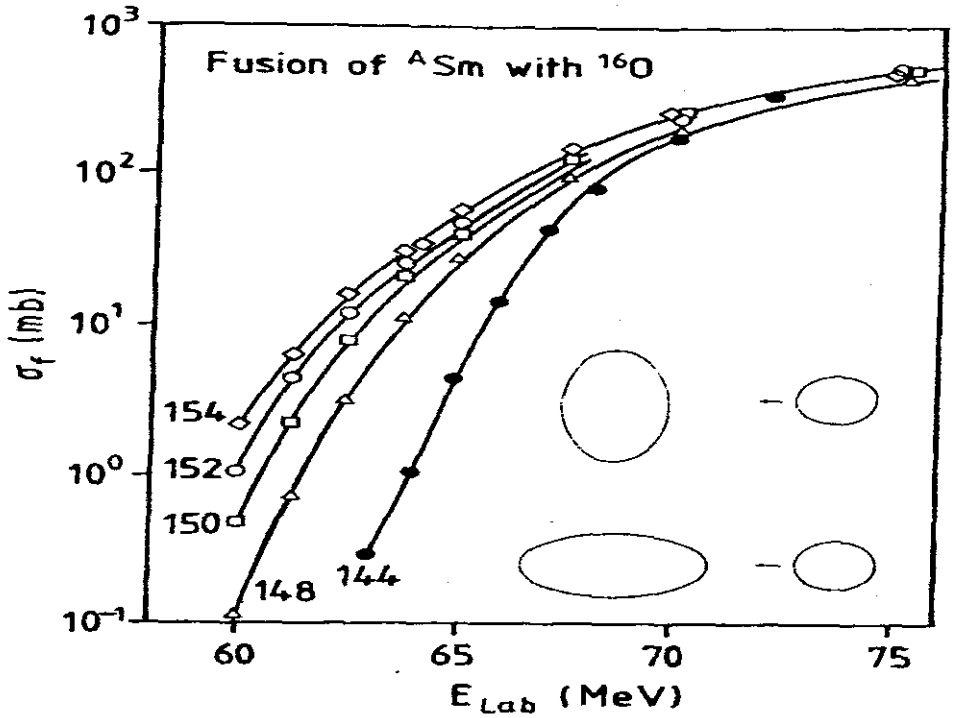

Figure 2-11: A collection of fusion data for ^{16}O on ^{A}Sm. The inset shows the orientations for which fusion is most inhibited and enhanced, from [Sto80].

2.5.1 Calculated and obtained experimental barrier distribution

The geometrical model predicts that for reactions involving rotational nuclei the one-dimensional Coulomb barrier is replaced by a continuous distribution of fusion barriers which correspond to the different mutual orientations of the projectile and the target nucleus. In this case the total fusion cross section is given by an integral over a continuous distribution of barriers $D(B)$, i.e.

$$\sigma(E) = \int \sigma(E,B) D(B) dB \qquad 2.23$$

where $\sigma_{fus}(E,B)$ is the fusion excitation function for the barrier B. The distribution $D(B)$ is a weighting function with the integral of the weights summing to unity.

$$\int_0^\infty D(B) dB = 1 \qquad 2.24$$

Therefore the barrier distribution is given by equation 2.25

$$\frac{1}{\pi R^2}\frac{d^2(E\sigma)}{dE^2} = \int G(E,B)D(B)dB \qquad 2.25$$

In the classical limit this gives the barrier distribution formula

$$\frac{1}{\pi R^2}\frac{d^2(E\sigma)}{dE^2} = D(E) \qquad 2.26$$

That is the quantity on the left hand side of this equation directly reproduces the barrier distribution $D(E)$. In the quantum mechanical treatment, which includes tunneling, the barrier distribution is smeared out by the Gaussian function $G(E,B)$, is symmetric about that point and has unit area. The only difference is its finite width. This concept can be extended by assuming that the coupling to internal degrees of freedom of the binary system generally gives rise to a multiple of fusion channels which correspond to a distribution of fusion barriers $D(B)$ [Ste88].

Precise experimental measurements of the excitation functions have allowed the extraction of the distribution of barriers $D(E)$ by taking the second derivative of the measured fusion cross-section using the point difference method, where the barrier distribution $D(E)$ defined as the probability of encountering a barrier of energy E, and can be determined directly from experimental fusion cross-sections [Row91, Lie95].

By measuring excitation functions, and by twice differentiating the excitation function multiplied by energy, experimental barrier distributions shown in figure 2.12 have been extracted. It can be seen from the experimentally measured barrier distribution that the $^{40}Ca + ^{40}Ca$ shows a single barrier due to the double closed-shell nature of the target and the projectile [Das98]. The barrier distribution for $^{16}O + ^{186}W$ and $^{16}O + ^{144,154}Sm$ shows the expected continuous barrier distribution for deformed targets. The three-barrier barrier structure in $^{56}Ni + ^{60}Ni$ are due to the surface vibration in this reaction.

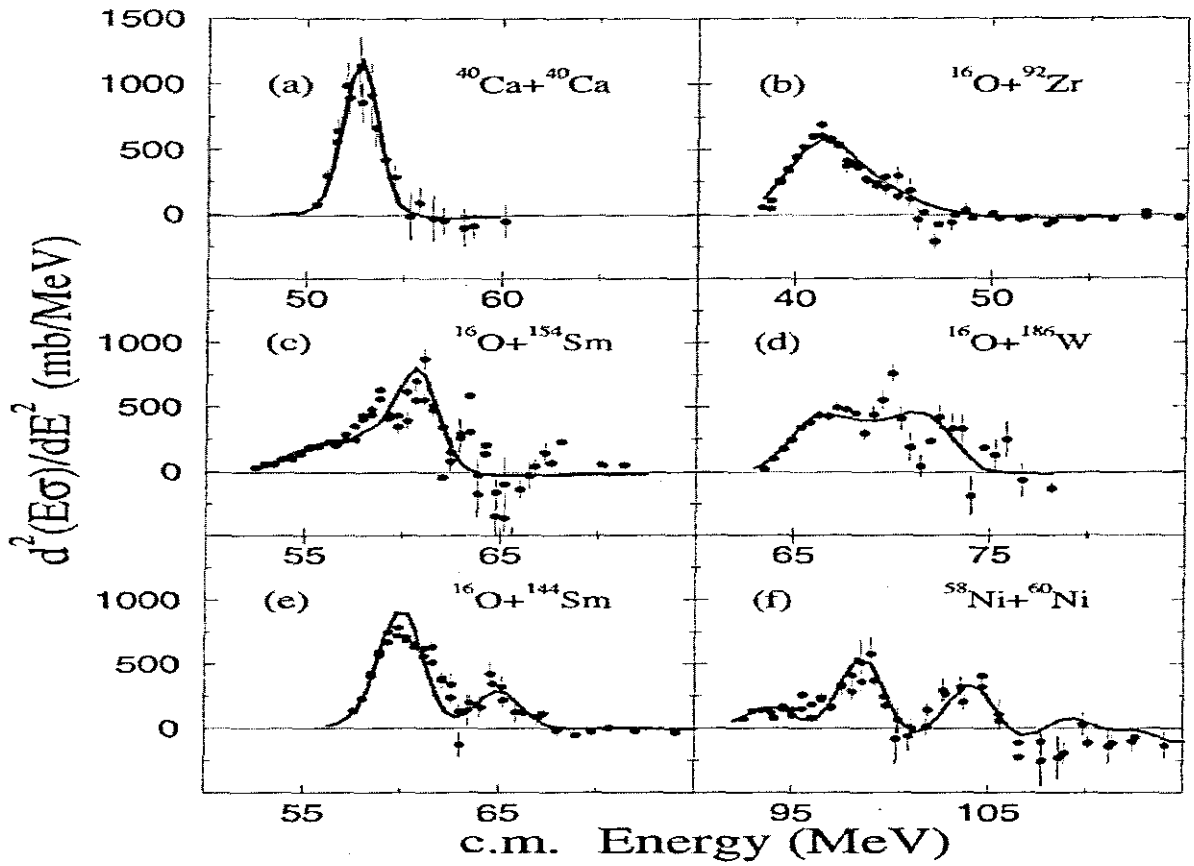

Figure 2-12: Experimental fusion barrier distribution for six different systems, from [Das98].

2.5.2 Extracting the barrier distribution from quasielastic scattering

In a purely classical picture in which projectiles incident on a target can only be elastically scattered or fused, there is a direct relationship between the fusion cross section and the elastic-scattering differential cross-sections, since any loss from the elastic channel contributes directly to fusion [Tim94]. For a single potential barrier B_k, and head-on collisions, for instance at the scattering angle $\theta = 180^\circ$, there is a direct relationship between the differential fusion cross-section $d\sigma^{fus}(E)$ and the quasielastic scattering differential cross-section $d\sigma^{qel}(E)$ [Tim04]. Flux conservation is given by equation 2.8. The reflected coefficient $R(E)$ is equal to the ratio of the differential cross-

section for quasielastic and Rutherford scattering $d\sigma^{qel}(E)/d\sigma^{R}(E)$, and the transmission coefficient may be written as the first derivative of the product of energy and total fusion cross-section $E\sigma^{fus}$ with respect to energy as explained by Balantekin et al., [Bal86]. i.e.

$$R(E)=\frac{d\sigma^{qel}}{d\sigma^{R}}\left(E,\theta=180^{\circ}\right) \qquad 2.27$$

$$\text{and } T(E)=\frac{1}{\pi R_0^2}\frac{d}{dE}\left[E\sigma^{fus}(E)\right] \qquad 2.28$$

Where R_0 is the inter-nuclear separation "fusion radius". The differentiation of $T(E)$ with respect to energy yields

$$\frac{dT}{dE}=\frac{1}{\pi R_0^2}\frac{d^2}{dE^2}\left[E\sigma^{fus}(E)\right]\equiv D(E,B_k) \qquad 2.29$$

The function $D(E,B_k)$ is the barrier distribution of the system, which for a single barrier is a δ-function at the barrier height B_k. Combining the equations 2.8, 2.27,2.28 and 2.29 it follows that

$$D(E,B_k)=\frac{dT}{dE}=-\frac{dR}{dE}=-\frac{d}{dE}\left[\frac{d\sigma^{qel}}{d\sigma^{R}}\left(E,\theta=180^{\circ}\right)\right] \qquad 2.30$$

Thus, classically for a single barrier, the barrier distribution $D(E,B_k)$ can be obtained by differentiating $\frac{d\sigma^{qel}}{d\sigma^{R}}(E)$ at 180^{0} with respect to energy. Quantum mechanically:

$$D^{fus}(E)=\frac{d^2}{dE^2}\left[E\sigma^{fus}(E)\right]=\pi R_0^2 G^{fus}(E,B_k) \qquad 2.31$$

which is the representative of the barrier distribution $D(E,B_k)$, because $G^{fus}(E,B_k)$ which is narrow peak function can also be 2.30, therefore it follows that;

$$D^{qel}(E)=-\frac{d}{dE}\left[\frac{d\sigma^{qel}}{d\sigma^{R}}\left(E,\theta=180^{\circ}\right)\right]=G^{qel}(E,B_k) \qquad 2.32$$

Using this equation the barrier distribution can be extracted from the quasielastic scattering at backward angles.

2.6 COUPLED-CHANNEL EFFECTS

When two nuclei approach each other they may interact in several ways. In the first approximation they may be regarded as a cluster of nucleons and their primary interaction results from the inter-nuclear two body-force. Nevertheless one or more rearrangement processes may occur during the time in which the reacting nuclei are together during collision. Inelastic excitations may occur, for example one or both of the reacting nuclei may be excited to higher energy states before fusion takes place [Tam65]. Rotational and vibrational excitations must be considered, and when the particle in one of the nuclei is excited during the reaction from its initial state to another state, single particle excitation may occur. Nucleons may also transfer from one nucleus to the other, either singly or as the simultaneous transfer of two or more nucleons. These processes are called multi-step reactions [Fes92]. The single step processes have been described by the Distorted Wave Born Approximation (DWBA), but in order to predict the effects of multi-step reactions, the coupled-channels formalism has been developed.

It has been found that coupling can greatly affect the fusion cross section [Das83]. It might be expected that the competition with other reaction channels would decrease the fusion cross-section, but one invariably finds an increase at energies below the barrier [Den00a]. These couplings result in a distribution of Coulomb barriers, whose energy spread increases with the coupling strengths. This in turn, generally leads to enhancements of the barrier crossing probability at low energies below the unperturbed Coulomb barrier.

2.6.1 Solution of the coupled equations

Consider a system comprising a beam and a target nucleus. The total Hamiltonian is given by

$$H = \frac{p^2}{2m} + V(r) + \sum_{i=0}^{\infty} \left(h_i(\alpha_i) + v_i(r, \alpha_i) \right) \qquad 2.33$$

where $\frac{p^2}{2m}$ represents the kinetic energy of the two nuclei and $V(r)$ the barrier between them. The h_i represent the Hamiltonian of the internal degrees of freedom of these nuclei and $v_i(r,\alpha)$ are the couplings between them. The nuclear coupling Hamiltonian is given by:

$$V_N(r,\hat{O}) = -\frac{V_0}{1+\exp\left((r-R-\hat{O})/a\right)} \qquad 2.34$$

where $\hat{O}$ can be a rotational or a vibrational coupling operator. E.g. the virational coupling operator is given by:

$$\hat{O} = \frac{\beta\lambda}{\sqrt{4\pi}} R_t(a^+_{\lambda 0} + a_{\lambda 0}) \qquad 2.35$$

where λ is the multipolarity of the vibrational mode [Hag99] and $a^+_{\lambda 0}(a_{\lambda 0})$ creation (annihilation) operator of the phonon. Then if χ_i satisfies the Schrödinger equation $[h_i - \epsilon_i]\chi_i = 0$ and form a complete orthonormal set of states with

$$\int \chi^*_j(\alpha_j)\chi_i(\alpha_i) = \delta_{ji} \qquad 2.36$$

we can expand the solution, Ψ, of the Schrödinger equation $H\Psi = E\Psi$ as

$$\Psi = \sum_i \phi_i(r)\chi_i(r,\alpha_i) \qquad 2.37$$

Inserting the wave function Ψ and the Hamiltonian equation into the Schrödinger equation yields the coupled equations

$$\sum_{i=0}^{n}\left[-\frac{\hbar^2}{2m}\frac{d^2}{dr^2} + V(r) + v_i^{coup}(r,\alpha_i) + \frac{l(l+1)}{2mr^2} - E + \epsilon_i\right]\phi_i(r)\chi_i(r,\alpha_i) = 0 \qquad 2.38$$

where ϵ_i is the excitation energies of the internal degrees of freedom.

If equation 2.38 is multiplied by $\chi^*_j(\alpha_j)$ and integrated over α_i for all i, the orthogonality property of equation 2.36 of the eigen-functions can be applied [Lin84]. One obtains the following system of coupled equations

$$\left[T_i + V(r) - E + \epsilon_i\right]\phi_j(r) = -\sum_{i=0}^{n} M_{ji}(r)\phi_i(r) \qquad 2.39$$

where $M_{ji}(r) = \int \chi_j^*(\alpha_j) v_i^{coup}(r,\alpha_i)\chi_i(\alpha_i)d\alpha_i + \epsilon_i\delta_{ji}$ 2.40

In the isocentrifugal approximation, the kinetic energy operator T_i depends on the channel angular momentum l_i through the centrifugal term [Das98]. This results in only a small discrepancy in an average angular momentum l_i such that T_i can be approximated to T_0. It has been explained that for heavy system such as $^{86}Kr + ^{208}Pb$ this is a good approximation due to the fact that there is a large mass and barrier radius [Smi83]. Further using an adiabatic approximation the excitation energies of the internal degree of freedom, ϵ_i may be neglected [Tim94] and $M_{ji} = \Gamma_{ji}F(r)$

$$(T_0 + V(r) - E)\phi_j(r) = -\sum_{i=0}^{n} M_{ji}(r)\phi_i(r) \qquad 2.41$$

Choosing the unitary transformation U_{jk}, to diagonalize the coupling matrix Γ_{ji} gives

$$U^+_{j\beta}\Gamma_{ji}(r)U_{i\alpha} = \Lambda_\beta\delta_{\alpha\beta} \qquad 2.42$$

In order to de-couple equation 2.41, the radial wave function ϕ_j may be expressed as

$$\phi_j(r) = U_{j\beta}\tilde{\phi}_\beta(r) \qquad 2.43$$

where Einstein's convention, that repeated indices imply a summation, is used. The inverse of equation 2.43 is

$$\tilde{\phi}_\beta(r) = U^+_{\beta j}\phi_j(r) \qquad 2.44$$

Substituting equation 2.43 into 2.39 yields

$$(T_0 + V(r) - E)U_{j\beta}\tilde{\phi}_\beta(r) = \Gamma_{ji}(r)F(r)U_{i\alpha}\tilde{\phi}_\alpha(r) \qquad 2.45$$

Multiply both sides by $U^+_{\beta j}$, where $U^+_{\beta j}U_{j\beta} = 1$, equation 2.45 becomes

$$\left[T_0 + V(r) - E\right]\tilde{\phi}_\beta = U^+_{j\beta}\Gamma_{ji}(r)F(r)U_{i\alpha}\tilde{\phi}_\alpha(r) \qquad 2.46$$

Using equation 2.42, the coupled equation 2.41, decouples to yield a system of decoupled Schrödinger equations for the wave functions $\tilde{\phi}_\beta(r)$

$$\left[T_O + V(r) - E + \Lambda_\beta F(r)\right]\tilde{\phi}_\beta(r) = 0 \qquad 2.47$$

The de-coupled equation 2.47 can be solved for the eigen-functions $\tilde{\phi}_\beta(r)$ which correspond to the eigen-channels $\beta = 0,1,.....,n$. This eigen-function follows the boundary conditions that for large distances the incoming wave function is a plane-wave and the outgoing wave function is a radial-wave.

The elements of the scattering matrix for the physical reaction are then:

$$S_{i,0}^{phys} = U_{i\alpha}U_{0\alpha}^{+}\tilde{S}_\alpha \qquad 2.48$$

The total fusion cross section is given by

$$\sigma^f = \frac{\pi}{k^2}\sum(2l+1)T_l(E) \qquad 2.49$$

Hence in the case of only elastic scattering, the cross-section can be expressed as;

$$\sigma^f = \frac{\pi}{k^2}\sum_{l,i}(2l+1)\left(1-\left|S_i^l\right|^2\right) \qquad 2.50$$

Dropping the l superscript

$$\sum_\alpha |S_\alpha|^2 = \sum_\alpha S^+S = \sum \tilde{S}^+U_{k0}U_{k\alpha}^+U_{\alpha j}U_{jo}^+\tilde{S}_j \qquad 2.51$$

$$= \sum \tilde{S}_k U_{ko}\delta_{kj}U_{jo}^+\tilde{S}_j \qquad 2.52$$

$$= \sum |U_{k0}|^2\left|\tilde{S}_k\right|^2 \qquad 2.53$$

$$\sigma^{fus} = \frac{\pi}{k^2}\sum(2l+1)\left(1-W_k\left|\tilde{S}_k\right|^2\right) \qquad 2.54$$

Where $W_k \equiv |U_{0k}|^2$ are the weights with which the various eigen-channels contribute to the fusion cross section. It is worth mentioning that the sum of all the weight is unity.

$$\sigma^{fus} = \sum W_k \sigma_R^{fus} \qquad 2.55$$

As the adiabatic approximation was used to obtain the cross-section, therefore if the energy of the excited state is taken into consideration equation 2.54 becomes incorrect.

CHAPTER 3 THE EXPERIMENT

3.1 EXPERIMENTAL ADVANTAGES OF MEASURING QUASIELASTIC SCATTERING

The quasielastic scattering of heavy ions at large angles has been proposed as an alternative method to extract the fusion barrier distribution [Tim95]. It has been studied both experimentally [Pia02] and theoretically. There are certain experimental advantages to this method. That is, one does not need to be concerned about the complex processes which may occur once the barrier has been crossed since it measures the flux scattered back from the barrier. An advantage of measuring quasielastic scattering is that it requires simple detectors since great resolution in mass, charge or energy is not needed. This has been exploited by Piaseck et al., [Pia02] for relatively light systems using PIN diodes. A further advantage of this method is that the use of detectors at different angles allows one to study the reaction at different effective energies without changing the beam energy.

In the semi classical approximation, each scattering angle corresponds to scattering at a certain angular momentum. To some extent the effective angular momentum can be corrected by shifting the energy by an amount equal to the centrifugal potential as shown in figure 3.1. Estimating the centrifugal potential at the Coulomb turning point R_C the effective energy may be expressed as:

$$E_{eff} = E - \frac{l_g^2(\theta)}{2mR_C^2} \qquad 3.1$$

Where $l_g(\theta) = \eta \cot(\theta/2)$ 3.2

Where θ is the scattered angle as shown in figure 3.2, and η is the Sommerfield [Fes92] or Rutherford parameter given by

$$\eta = \frac{Z_p Z_t e^2}{4\pi\epsilon_0 \hbar v} \qquad 3.3$$

In this equation Z_t, Z_p are the charges of the target and the projectile respectively, and e is the unit of charge.

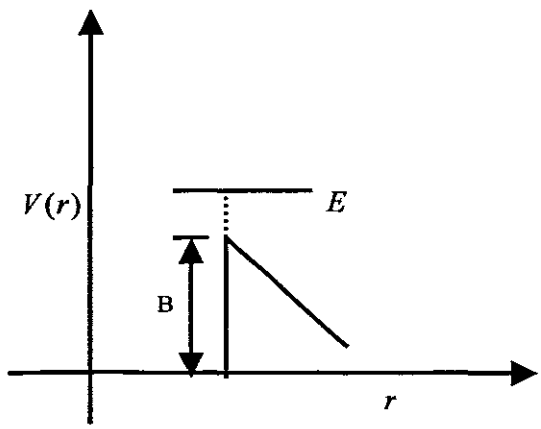

Figure 3-1: The Sharp cut off approximation estimated by Wong.

The scattering angle and the impact parameter directly affect both the fusion cross-section and the effective energy of the system.

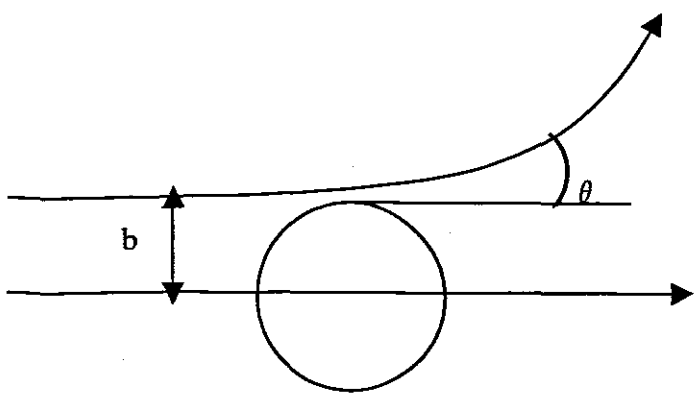

Figure 3-2: Illustration of the scattered particle with the impact parameter b at an angle θ.

Substituting the Sommerfield parameter, equation 3.3 and the angular momentum equation 3.2 in equation 3.1 yield;

$$E_{eff} = E - \left(\frac{Z_p Z_t e^2}{4\pi\epsilon_0 R_c}\right)^2 \left(\frac{1}{\hbar v}\right)^2 \frac{1}{2m}\hbar^2 \cot^2(\theta/2) \qquad 3.4$$

Since the mapping of interest is the one where the effective energy is equal to the barrier,

$$E_{eff} = B \qquad 3.5$$

where E_{eff} is the effective energy and B is the barrier.

Therefore equation 3.1 becomes

$$E_{eff} = E - \frac{E_{eff}^2}{4E}\cot^2(\theta/2) \qquad 3.6$$

Which simplifies to the formula of the effective energy

$$E_{eff} = \frac{2E}{1+\cos ec(\theta/2)} \qquad 3.7$$

Before the experiment was done, this formula was used to predict the most effective and efficient way of performing the experiment. This was done by calculating the effective energies for the entire scattering angle range between 140°and 180°. The effective energies were computed in mapping steps of about 0.2 MeV as shown in figure 3.3.

This not only improves the efficiency of the experiment but also allows the use of a cyclotron accelerator where the relatively small energy steps required for barrier distribution experiment cannot be obtained from the cyclotron itself. The Barrier distribution was in the past obtained by second derivative as a function of energy $d^2(E\sigma)/dE^2$ [Row91]. However, when measuring quasielastic excitation functions the barrier distribution is given by

$$D(E_{eff}) = -\frac{d(\sigma_{QE}/\sigma_R)}{dE_{eff}} \qquad 3.8$$

where E_{eff} is the effective energy given by equation 3.7. Andres et al., [And88] suggested this alternative method to determine fusion barrier distribution. This needs less accuracy in the data since the first derivative gives the barrier distribution rather than the second derivative.

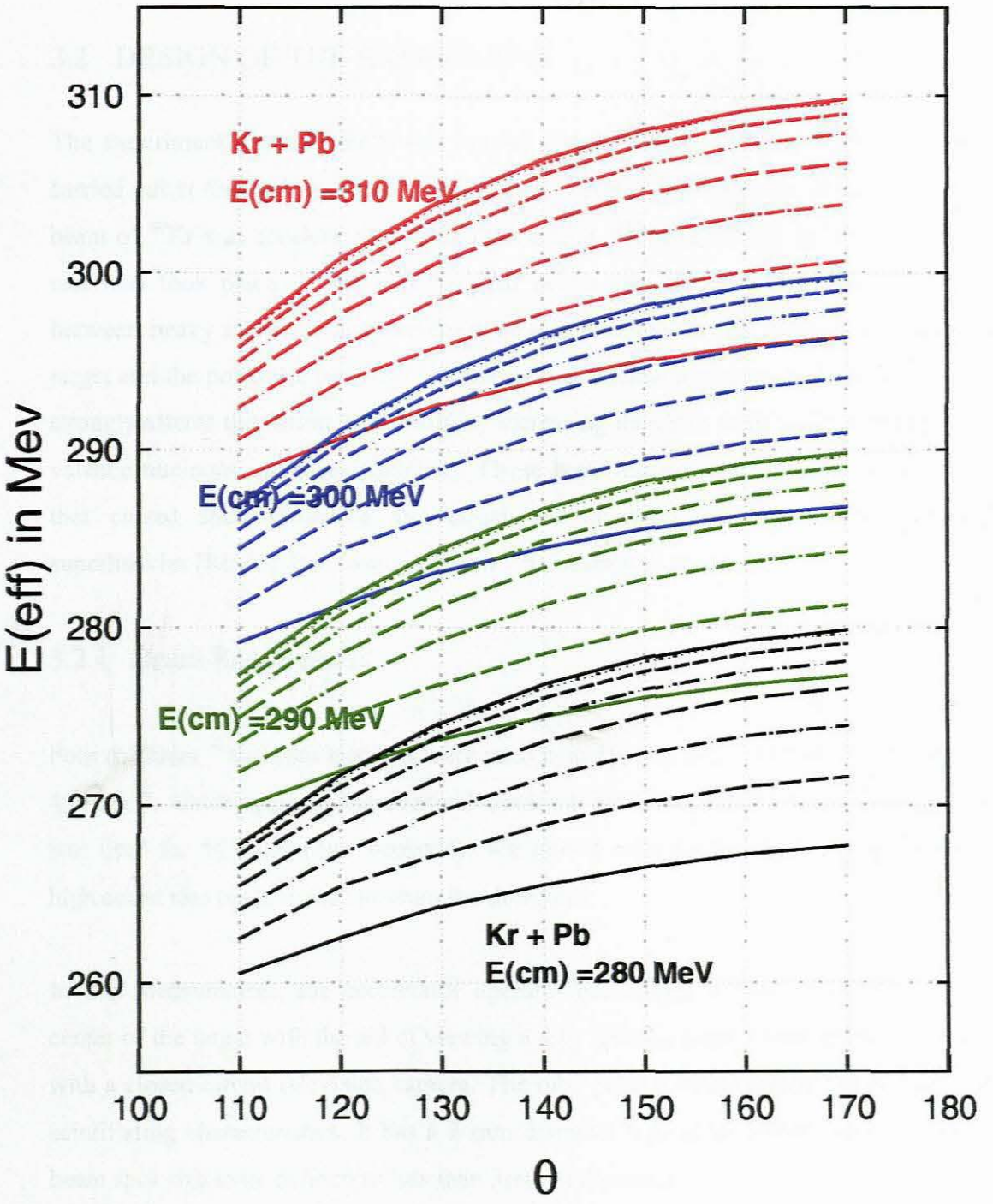

Figure 3-3: The illustration of the conversion of the beam energy to the effective energy as a function of the angle of the arm.

3.2 DESIGN OF THE EXPERIMENT

The experiment to study the fusion barrier distribution for $^{86}Kr + ^{208}Pb$ reaction was carried out at the cyclotron facility at iThemba LABS, South Africa. In the experiment a beam of ^{86}Kr was accelerated and directed onto a ^{208}Pb target foil in which the nuclear reactions took place. It has been pointed out in the literature that fusion probability between heavy nuclei at low excitation is also sensitive to the nuclear structure of the target and the projectile [Qui93]. The number of valence nucleons in the outer most shell strongly affects the fusion probability by increasing the extra push as the number of these valence nucleons increases [Sch91b]. These have made scientists draw the conclusion that closed shell projectile and target are favorable candidates for synthesizing superheavies [Ria00]. For these reasons a ^{86}Kr beam was choosen.

3.2.1 Beam Requirement

Four different ^{86}Kr beam energies were used namely, 396 MeV, 410 MeV, 438 MeV and 450 MeV, which spanned the classical Coulomb barrier at 420 MeV. Each beam energy was used for 56 hours (one weekend). We started with the 396 MeV energy, where the high count rate made it easy to setup the detectors.

In this measurement, the accelerator operator maintained a focused beam spot at the center of the target with the aid of viewing a ruby (Al_2O_3) target in the scattering chamber with a closed-circuit television camera. The ruby gives a visual indication of halo due its scintillating characteristics. It has a 3 mm diameter hole at its center, which allows, the beam spot size to be defined to less than 3mm in diameter.

3.3 TARGETS

Various self-supporting target foils were used during the course of this work. The target used and the target thicknesses are summarized in table 3.1. Figure 3.4 illustrates the dimensions of the aluminum target ladder, which can hold five aluminum target frames.

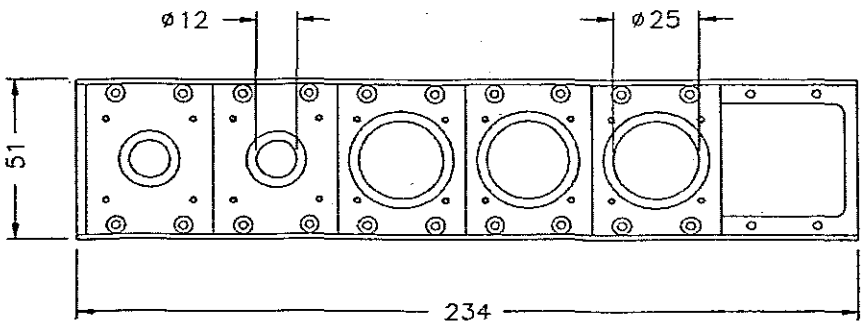

Figure 3-4: Top view of the horizontal representation of the target ladder illustrating the two different target holders mounted at five target positions.

The dimensions are in mm and the drawing scale is 1:2.

Target	Thickness in μgcm^{-2}
^{208}Pb	50
^{208}Pb	100
Empty	
Al_2O_3	100
Au	100

Table 3-1: The targets used in this experiment.

The edge of the target frame where the ^{208}Pb target was mounted was attached with small magnets to ensure that electrons were deflected away from the detectors, since electrons could harm the silicon surface barrier detector and photovoltaic cells, detectors that were used in this experiment. First a $100\mu gcm^{-2}$ self supporting Pb target was used but due to

the low melting point of ^{208}Pb, this target did not last long, it broke with only 0.143pnA of ^{86}Kr beam on the very same weekend. As a result, the target used in this measurement was made of a sandwich of 50 μcm^{-2} of ^{208}Pb between 50 μcm^{-2} and 10μcm^{-2} of ^{12}C. The energy lost in the target was 3.6 MeV. Since the ^{208}Pb is very easy to melt, a Gold (*Au*) target was used to set up the electronics, since it has a higher melting point, is a very good conductor, and is not easy to melt during the testing process. The main purpose of the empty target was to measure the detector and electronic noise with the beam on.

3.4 SCATTERING CHAMBER

The experiment was performed in the 1.5 m diameter scattering chamber which is located in the A-line at iThemba LABS. The chamber has two independently movable detector arms to which the detectors, preamplifiers etc can be attached. The target mechanism at the center of the scattering chamber makes provisions for a target ladder, which holds five different targets vertically aligned above one another. By remotely changing the height of the ladder, any of the five targets can be positioned in the beam. The target ladder can also be rotated about its own vertical axis to select the target angle with respect to the beam direction. The wall of the scattering chamber is well equipped with several ports, which are used for various purposes. One port situated just above the beam entrance is fitted with a perspex window to allow a closed-circuit television camera to monitor the beam spot, which is produced by a scintillating target i.e. ruby Al_2O_3. The other ports provide feed throughs for 50Ω and 93Ω BNC cables; high voltage (SHV) cables and power supply cables used for the preamplifiers and detectors, which are mounted in the chamber. Some of the ports, which accommodate BNC and SHC cables, are located in the lid of the chamber. All the movable components inside the chamber, for example, detectors arms and target ladder holder, can be moved to different angles with respect to beam direction, using remote controls which are located both inside the chamber vault and in the data room.

SCATTERING CHAMBER

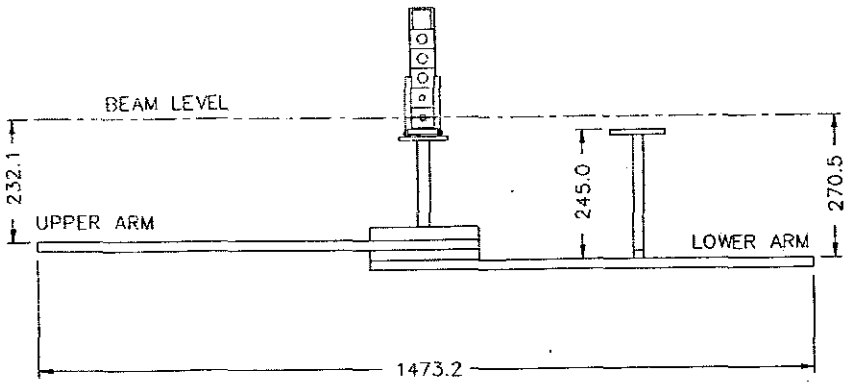

Figure 3-5: Side elevation of the movable set-up inside the scattering chamber that includes the vertically adjustable and rotatable target holder in the center and both detector arms with one detector stand for display. The dimensions are in mm and the drawing scale is 1:10.

A patch panel situated next to the scattering chamber, which is connected to a similar panel in the data acquisition room, provides separate insulated 50Ω BNC, 93Ω BNC and SHV connections. Cable input to, and output from, the scattering chamber are connected via the patch panel. Before any measurement can be done the scattering chamber had to be pumped down to 10^{-5} mbar. This vacuum can be obtained by using three different types of pumps. It is important to make certain that the O-ring is clean and is sealed properly if the lid has been open. Initially, a rotary pump was used to pump the chamber down to 10^{-1}mbar, followed by a turbo molecular pump that took it down to a pressure 10^{-3}mbar. Lastly, the Cryogenic pump was used to pump the scattering chamber down to the required pressure of 10^{-5} mbar. The operating temperature for the Cryogenic pump is specified to be less than 24K. Before the experiment, the pumping down took about 1.5 hrs. After all the measurements were completed the vacuum in the scattering chamber was found to be 80×10^{-5} mbar. Whenever the scattering chamber had to be opened (for example to check if the target was still in good condition or to change the target) dry Nitrogen gas had to be used to break the vacuum, which helped to speed up the pump down process.

3.5 DETECTORS

The photovoltaic cells and a silicon surface-barrier detector were the only detectors which were used in this experiment. The twenty-five photovoltaic cells were arranged in the detector holder as shown in figure 3.6.

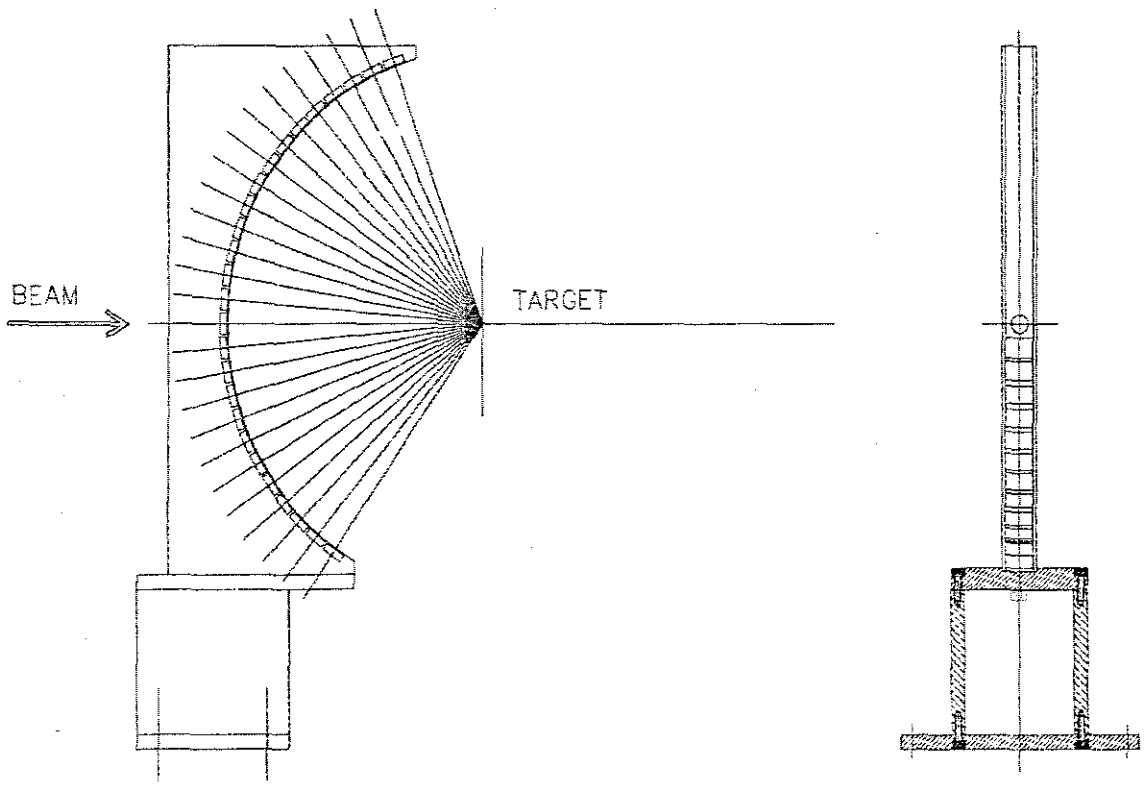

Figure 3-6: The twenty-five photovoltaic cells in the detector holder illustrating the geometric layout of the photovoltaic cells relative to the beam direction.

In the middle of the detector holder, there is a hole, which was made to allow the beam to pass through to the target. On top of the hole there were fourteen photovoltaic cells and there were eleven photovoltaic cells below. The detector holder was designed such that the eleven photovoltaic cells on bottom of the hole are symmetric to the first eleven photovoltaic cells from the hole to the top, with respect to beam direction. The detector holder with twenty-five photovoltaic cells was attached to the upper arm at the backward

angle at a distance of 150 mm away from the target. Each photovoltaic cell was 9x10 mm^2 in active area, resulting in a solid angle of 6.6 msr.

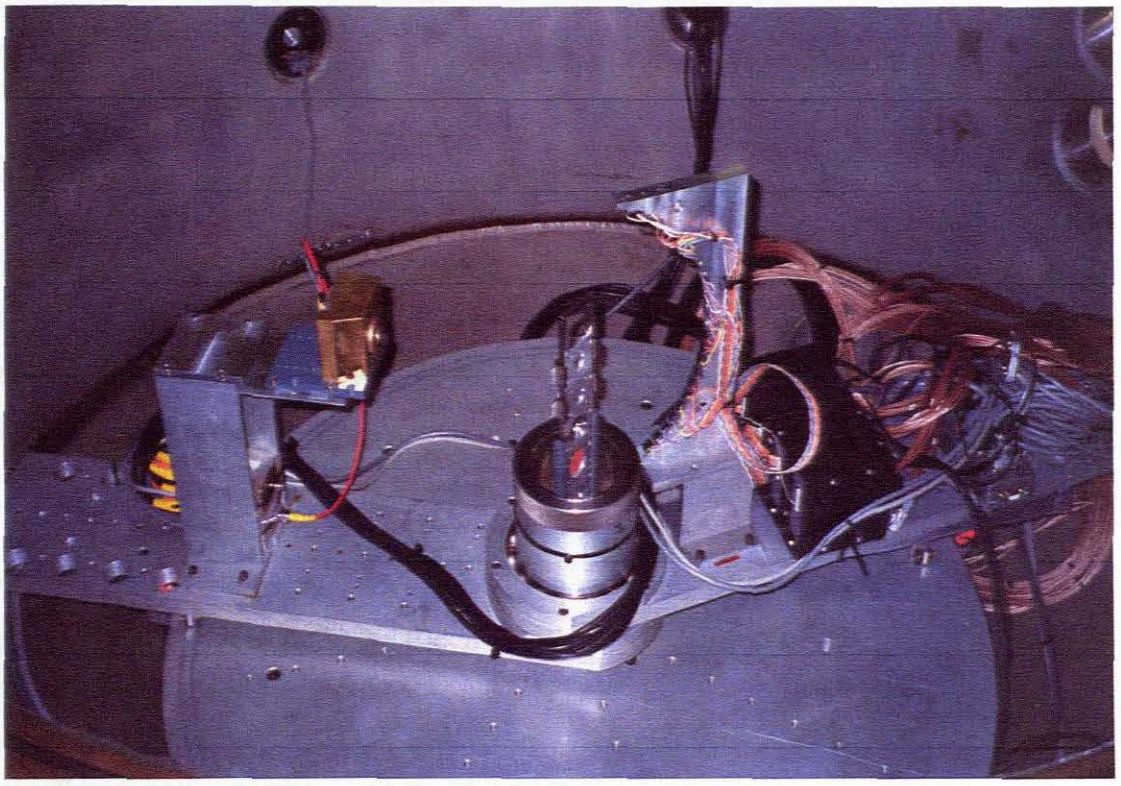

Figure 3-7: The experimental layout inside the 1.5m diameter scattering chamber illustrating the twenty-five photovoltaic cells in the detector holder which was shielded on the upper arm, the preamplifiers and the silicon detector inside the colliminator.

One reason for the photovoltaic cell arrangement was to acquire more data points; therefore, for each beam energy the angle θ of the upper arm was changed to different angles namely 140°, 155°, 160°, 170°, and 180°. The photovoltaic cells were placed such that they were at angles of 5° from each other. Therefore the angle of each photovoltaic relative to the beam direction was given by

$$\Phi = \cos^{-1}(\cos\theta\cos\psi) \qquad 3.8$$

where θ is the angle of an arm and ψ is an angle of an individual photovoltaic cell out of the plane defined by the beam and the centre of the photovoltaic array. On the other arm

there was a silicon-surface barrier monitor detector, which was inside a 1.38 cm diameter colliminator, located at 272.62 mm away from the target. Therefore the silicon-surface barrier detector subtended a solid angle of 2,02 msr to the target.

3.5.1 Photovoltaic cells

When an energetic ion passes through a material it predominately deposits energy via the Coulomb interaction with the material's electrons, therefore it looses some of its energy to electrons [Bra00]. The energy losses per unit path length in this process in the case of a heavy ion is approximated by the Bethe-Bloch equation

$$\frac{dE}{dX} \propto Zz^2 \qquad 3.9$$

where Z is the atomic number of absorbing material and z the charge of the incident particle in unit of e. The Bethe-Bloch equation shows that more energy can be lost by an ion per unit distance if the atomic number is large; hence more electrons are liberated if a heavy ion passes through the material. The photovoltaic cells are semiconductors, to understand their operation, we begin by reviewing the physics of semiconductors.

In solid material electrons fill different bands with different energy. The last filled band is called the valence band and the next highest band is called the conduction band. The electrons that play a role in conduction, i.e. charge carriers, occupy the conduction band. Electrons in a filled band cannot move, but they can jump to the next higher band if they experience an appropriate energy. In a partially filled band electrons can move to occupy the free states. In an insulator the valence band is filled, and the gap between the conduction band and the valence band is big. The valence band in a semiconductor is partially filled and the gap between the valence and the conduction band is very small. In conductor materials the valence band is partially filled and the conduction band overlaps the valence band. Because of the small separation between conduction band and valence band in semiconductors, they behave like an insulator at low temperature $T = 0\,\mathrm{K}$, since there is no energy to raise electrons to the conduction band, but at high temperature

$T > 0\,\mathrm{K}$ they behave like conductors, since some of the electrons are raised by thermal energy into the conduction band. This behavior makes the semiconductor a suitable candidate in making photovoltaic cells. Semiconductors mainly have four electrons per atom in their valence band. They can be classified into n-type or p-type and n-p junctions.

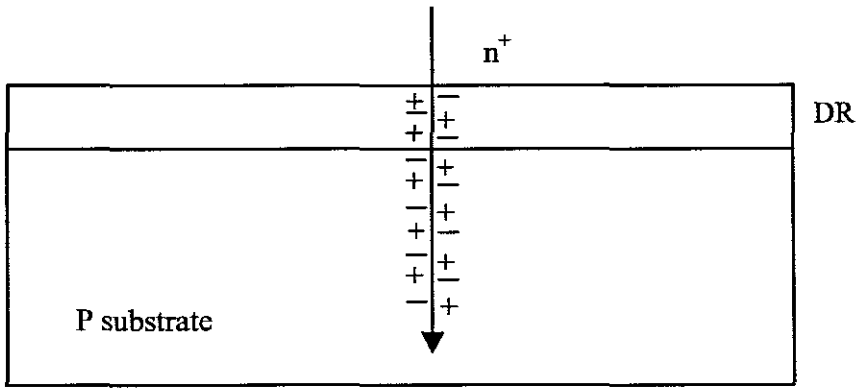

Figure 3-8:The illustration of the process that takes place when an ion passes through the depletion region of the photovoltaic cell.

The n-type material is the semiconductor that is doped with an impurity element that has five valence electrons, where four bond with other atoms from the semiconductor i.e silicon and the other electron remains unbound in the material and plays a role in conducting. The p-type is the one doped with an impurity element with only three valence electrons, which bond with other three leaving one free hole which acts as a charge carrier.

An n-p junction is formed when n-type and p-type materials are placed together. In the n-p junction the electrons moves from the n-type to the p-type and the holes move from the p-type to the n-type through the process of diffusion. The electrons that move across the boundary combine with the hole and the depletion region (DR) is formed as shown in figure 3.8.

Since they are designed for detecting photons, the depletion region is very thin. An energetic heavy ion will pass through the depletion region. The redistribution of charge caused by the ion track creates a "funnel" [Bra00] through which electrons flow into the depletion region to produce signal. The energy loss per unit path is proportional to the atomic number of the ion, hence there is more funneling for heavier ions since more hole-electron pairs would be created and collected by funneling. After the carriers in the funnel have been collected the depletion region returns to its stable state. Thus the photovoltaic cell is sensitive to heavy ions and fission fragments since they have high atomic number.

3.5.2 Silicon surface barrier detector

The silicon surface barrier detector was obtained form the Oak Ridge Technical Enterprises Corporation (ORTEC). In this detector, the center electrode of the connector is supplied with a positive bias potential and provides a negative output signal. The characteristics of the silicon-surface barrier detector are given below.

Active area (mm^2)	Shaping time Constant (μs)	Noise width keV (FWHM)	Sensitive Thickness (μm)	Electrode thickness ($\mu g.cm^{-2}$)		Sensitive Depth (min) μm	Bias Voltage (V)
				Au	Al		
300	0.5	9.1	27.6	40	40	31.2	20

Table 3-2: Properties of the silicon surface barrier detector.

Silicon surface barrier detectors rely on the junction formed between a semiconductor and certain metals, usually n-type silicon with gold or p-type with aluminium. The one used here was the one made of n-type silicon with gold. Because of the different Fermi levels in these materials, a contact emf arises when two are placed together. This cause a lowering of the band levels in the semiconductor as illustrated in figure 3.9.

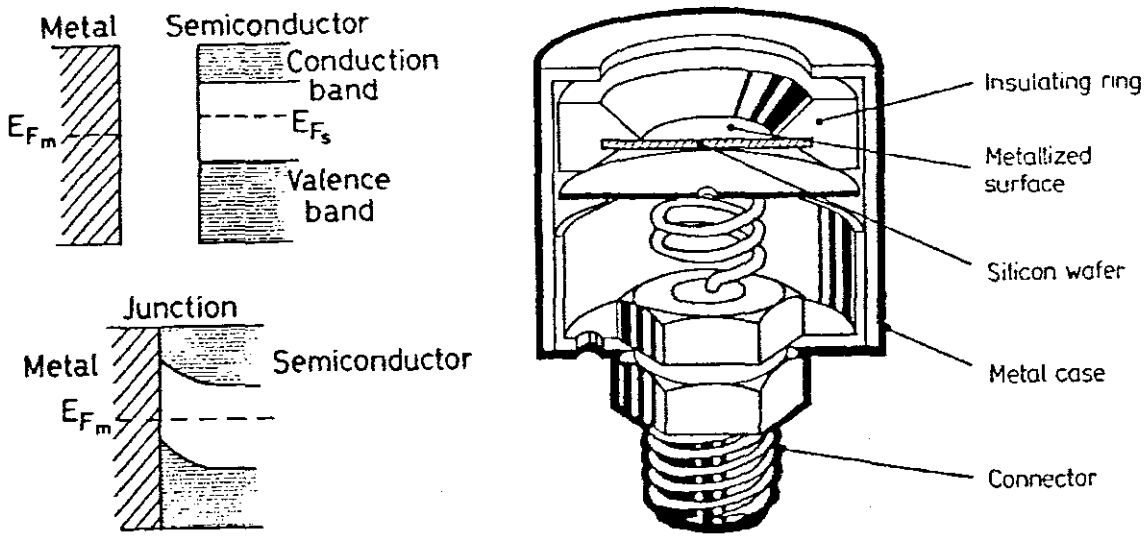

Figure 3-9: Formation of a Schottky barrier junction, and the schematic diagram of a surface barrier detector (from Ortec), from [Leo87].

This situation is similar to the np- junction and a depletion zone extending entirely into the semiconductor is formed. These junctions are also known as Schottky barriers and possess many of the characteristics of pn-junctions. The depletion depth in a surface barrier detector can be calculated using

$$d = x_n = \left(\frac{2\epsilon V_0}{eN_D}\right)^{\frac{1}{2}} \qquad 3.15$$

where ϵ is the dielectric constant, e is the charge of the electron, N_D is the donor impurity and V_0 is the pontential.

With current high resistivity silicon, depths of ~ 5 mm can be attained. Surface barrier detectors can be made with varying thickness and depletion zone regions.

If the detector is not too thick, a fully depleted detector is possible. In that case the depletion zone extends through the entire thickness of the silicon wafer. Furthermore by increasing bias on fully depleted detectors, a gain in the collection times of the charges

can be obtained resulting in a faster signal risetime. Like the photovoltaic cells, the silicon surface barrier is sensitive to light. The thick gold covering is insufficient to stop ambient light. Therefore, it was necessary to ensure that the inside of the scattering chamber was kept free of light.

3.6 ELECTRONICS AND DATA ACQUISITION

This section deals with the electronic setup used in this measurement. The output of the twenty-five photovoltaic cells and silicon monitor detector were each connected to their own preamplifier. The function of the preamplifier is to provide an interface between the detector and the pulse processing electronics; it serves as an impedance matcher by providing a high impedance to the detectors while providing a low impedance output to drive succeeding components, to amplify weak signals from the photovoltaic cells and to shape the subsequent output pulses. In order to reduce electronic noise, the preamplifiers were placed inside the scattering chamber, strapped to the upper arm, on which the detector holder with the twenty-five photovoltaic cells was mounted. Likewise in the lower arm the preamplifier was placed close to the Silicon surface barrier detector.

The linear output signals from the silicon preamplifier were fed to a 572 amplifier then to a linear gate and stretcher (LGS, Ortec model 542) then to the input of the 8077 NIM Analogue to Digital Converters (ADC), (Canberra model 8077) (see figure 3.10). In order to obtain a logic signal from the silicon detector, a second output from the preamplifier was fed into the input of the timing filter amplifier (TFA 474), and then followed by a constant fraction discriminator (CFD 934), which produced a fast logic pulse (see figure 3.11).

The output signal from each of the twenty-five photovoltaic cell preamplifier was fed to sixteen channel CAEN N568 amplifiers which were used to supply both energy and timing signals. The energy signal would be subsequently measured in the Silena 4418 ADC (see figure 3.12); the timing signals were intended for gating of the ADC's and

dead time corrections. However, the photovoltaic cells proved to be vulnerable to pick up of high frequency noise, evidently generated by the turbo molecular pumps, and it proved to be impossible to use constant fraction timing. This did not affect the linear signals, which could use a large shaping time to integrate the noise out. Instead, the linear signals were also used to generate timing signals to gate the ADC's.

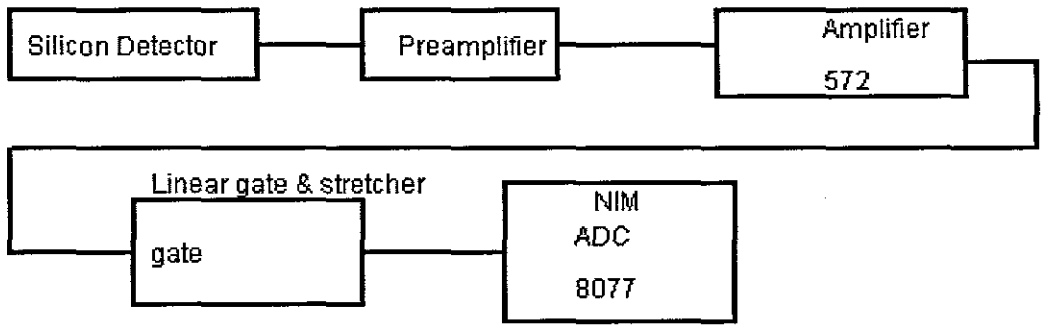

Figure 3-10: The electronic diagram for linear signals from the silicon surface-barrier detector.

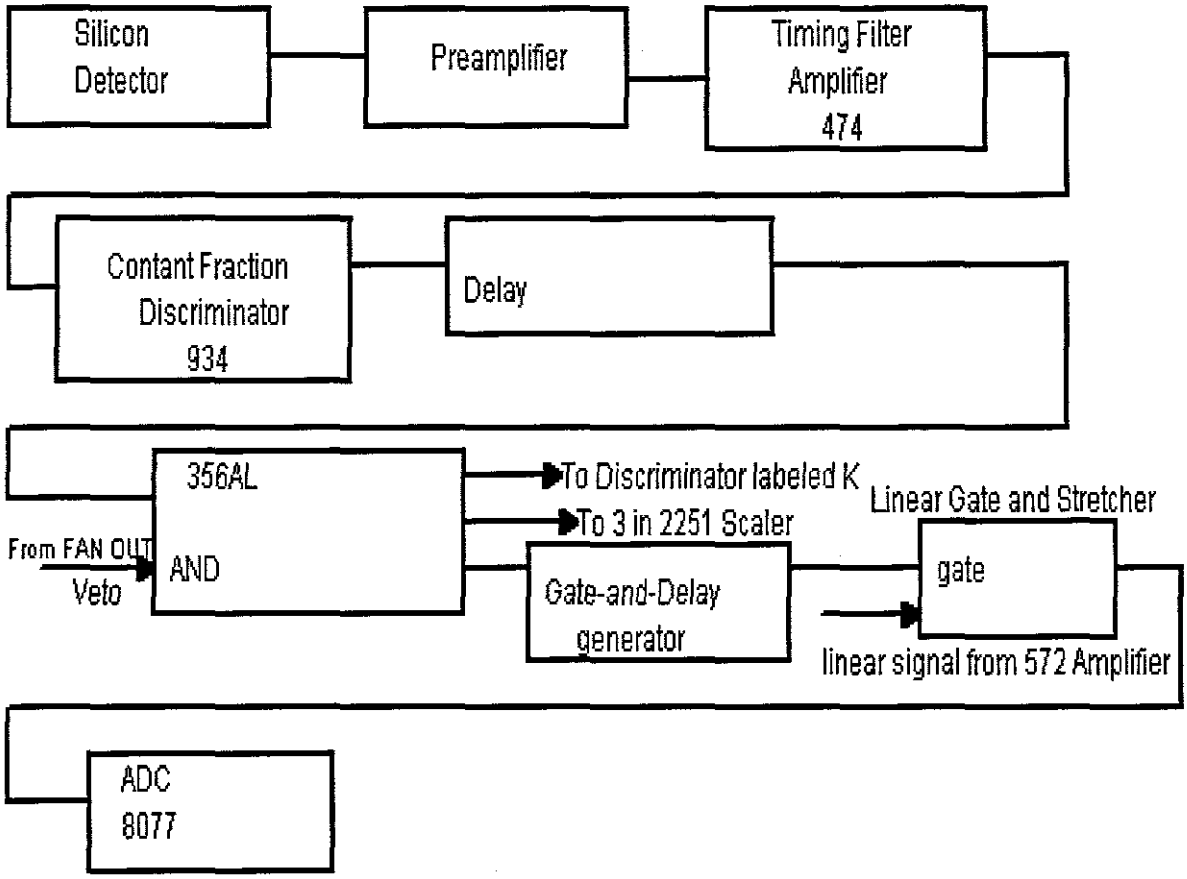

Figure 3-11: The simplified electronic diagram for timing signal from the silicon surface-barrier detector.

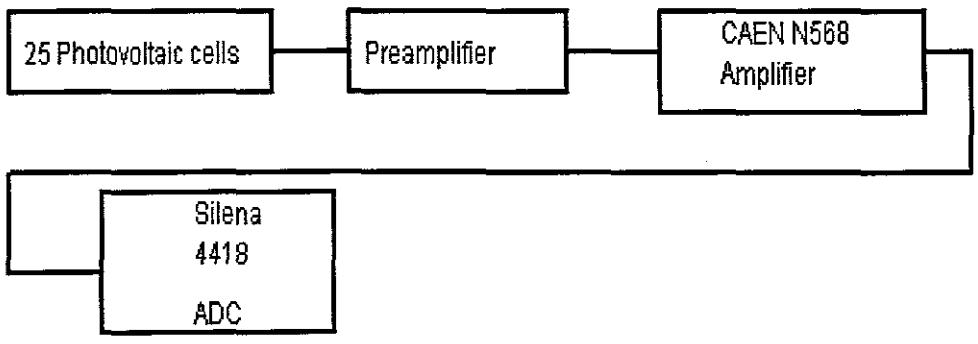

Figure 3-12: The electronic diagram for linear signals of the twenty-five photovoltaic cells.

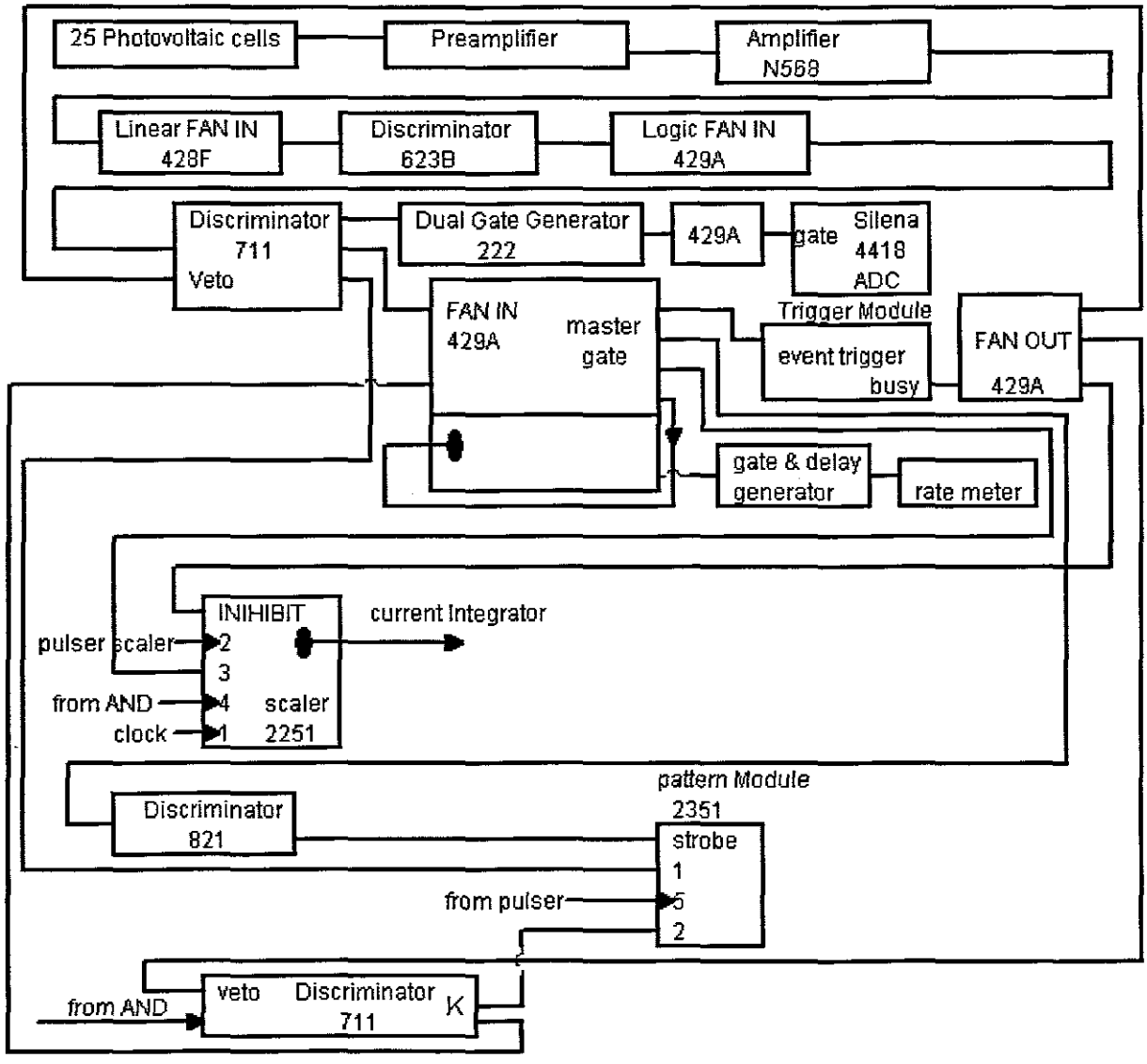

Figure 3-13: The simplified electronic diagram for timing signal from the twenty-five photovoltaic cells.

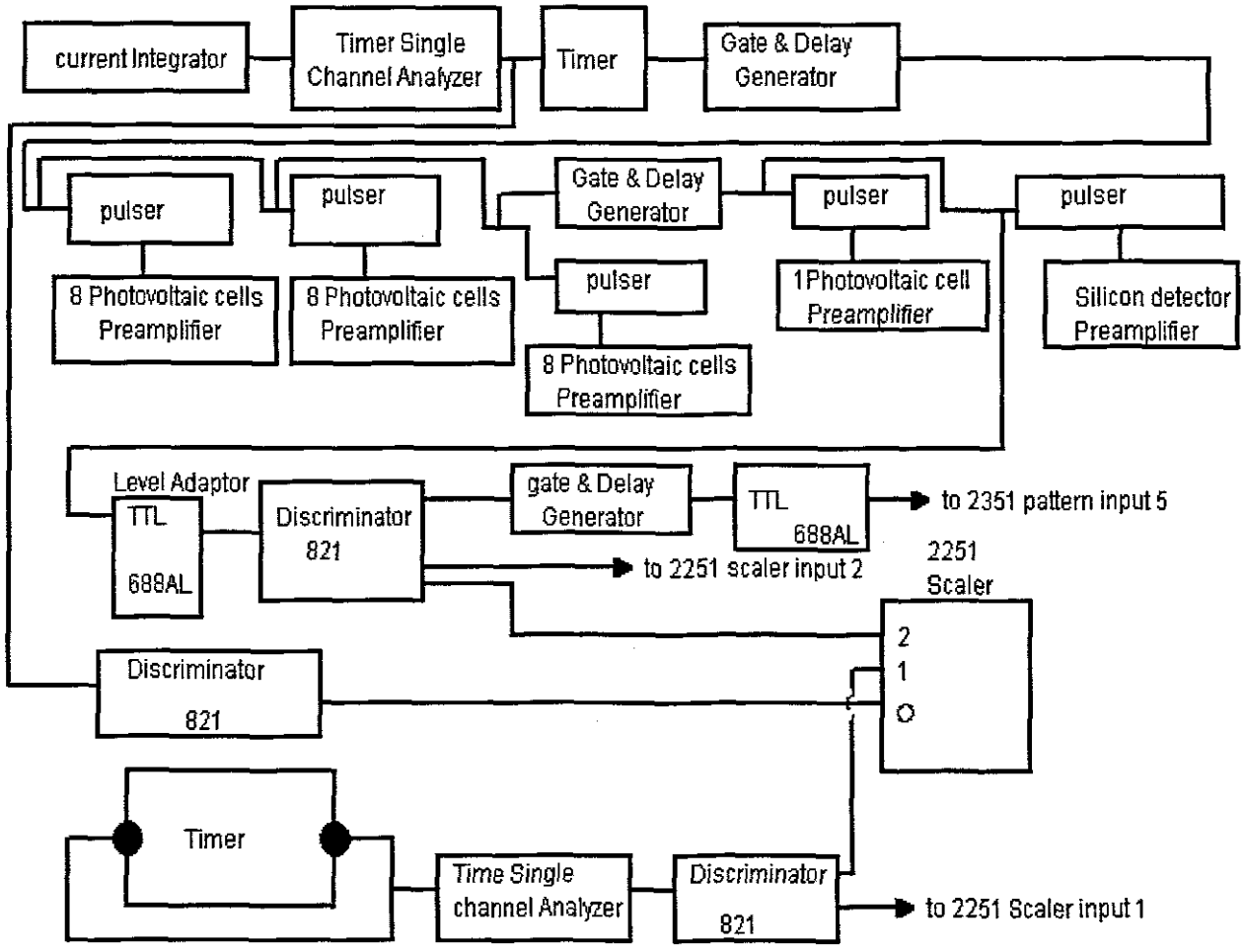

Figure 3-14: The separate circuitry for the current integrator and pulsers.

The twenty-five timing signals were fanned in to produce a trigger signal at the 711 Discriminator. This signal gated the Silena 4418 ADC, and was then fanned in together with the gating signal from the silicon monitor detector to produce a master gate that activated the trigger module. The trigger module would initiate CAMAC and NIM read out of the ADC's. At the same time, the computer busy signal would inhibit further acquisition by fanning out to veto inputs of the 711 discriminator (photovoltaic) and the linear gate of the silicon detector (figure 3.11).

Dead time correction was made by injecting pulser signals, scaled by the beam current, into the photovoltaic and the silicon surface barrier detector preamplifiers, as shown in figure 3.14. The function of the scalar is to count the number of events. One of these scalars was inhibited by the computer busy signal as shown in figure 3.13. The uninhibited scalar was linked directly to the electronic clock. By comparing the uninhibited and the inhibited scalar readings during data acquisition, an estimate of the dead time could be made. The dead time of individual detectors could be estimated by comparing the number of pulser events recorded in the detector spectra with the scaler.

However because of the poor timing of the photovoltaic logic signals, the veto could arrive at the wrong time at the linear gate, which resulted in errors in the scalers and in dead time correction. This issue is further addressed in section 4.6.2. The purpose of the pattern module (figure 3.13) was to register the type of event (e.g. the origin of a specific event), for example whether it is an event from the photovoltaic cell or it is a pulser or a non-pulser event.

3.6.1 Data Handling

The VME is the interface to the VAX data computer and this VAX did the online data handling analysis. More details about the VME has been explained by John Pilcher in [Pil96] and N.R Yoder in [Yod94]. All the software used to control the data is from the XSYS system, which runs on the VAX VMS operating system. In XSYS, two program files are run to handle data, namely the COM file and the EVAL file. The COM file creates all the necessary data areas for the data to be stored (this includes data areas of graphs). The EVAL code uses these data areas to sort and analyze the raw data from the buffers. These raw data are stored to disk in data files and can be played back with various software and offline sorting routines at a later stage to analyze the data, by using the same COM and EVAL files. The EVAL file also does verification and analyzing of the events. The EVAL files for this experiment were written by Dr. S.V. Förtsch.

CHAPTER 4 DATA ANALYSIS

4.1 DATA ANALYSIS

The count rate of the photovoltaic cells was decreasing with increasing scattering angle relative to the beam direction. A very clean spectrum was obtained at 396 MeV, which is 20 MeV below the Coulomb barrier of ^{86}Kr and ^{208}Pb. This was an indication of pure Rutherford scattering. Figure 4.1 shows some examples of spectra obtained from a photovoltaic cell which at different angles and energies. Since the eleven photovoltaic cells below the plane were symmetric to the other eleven above, as it was explained in section 3.5, detectors which were at the same angles were expected to count at the same rate, as shown in figure 4.2. However, it was found for many runs that there were unexpected discrepancies between the top and bottom photovoltaic cell counts, as shown in figure 4.3. It was deduced that the discrepancies were caused by the beam being not well aligned, disrupting the symmetry. Furthermore, the first three top photovoltaic cells, which were not symmetric, were counting at an unexpected count rate. It was suspected that they were shadowed by the small magnets on the target frame, as this was more pronounced at low angles (for instance if the angle of the arm was at 140°). Therefore these three photovoltaic cells were not considered during the analysis; hence the analysis was done only with the twenty-two symmetric photovoltaic cells.

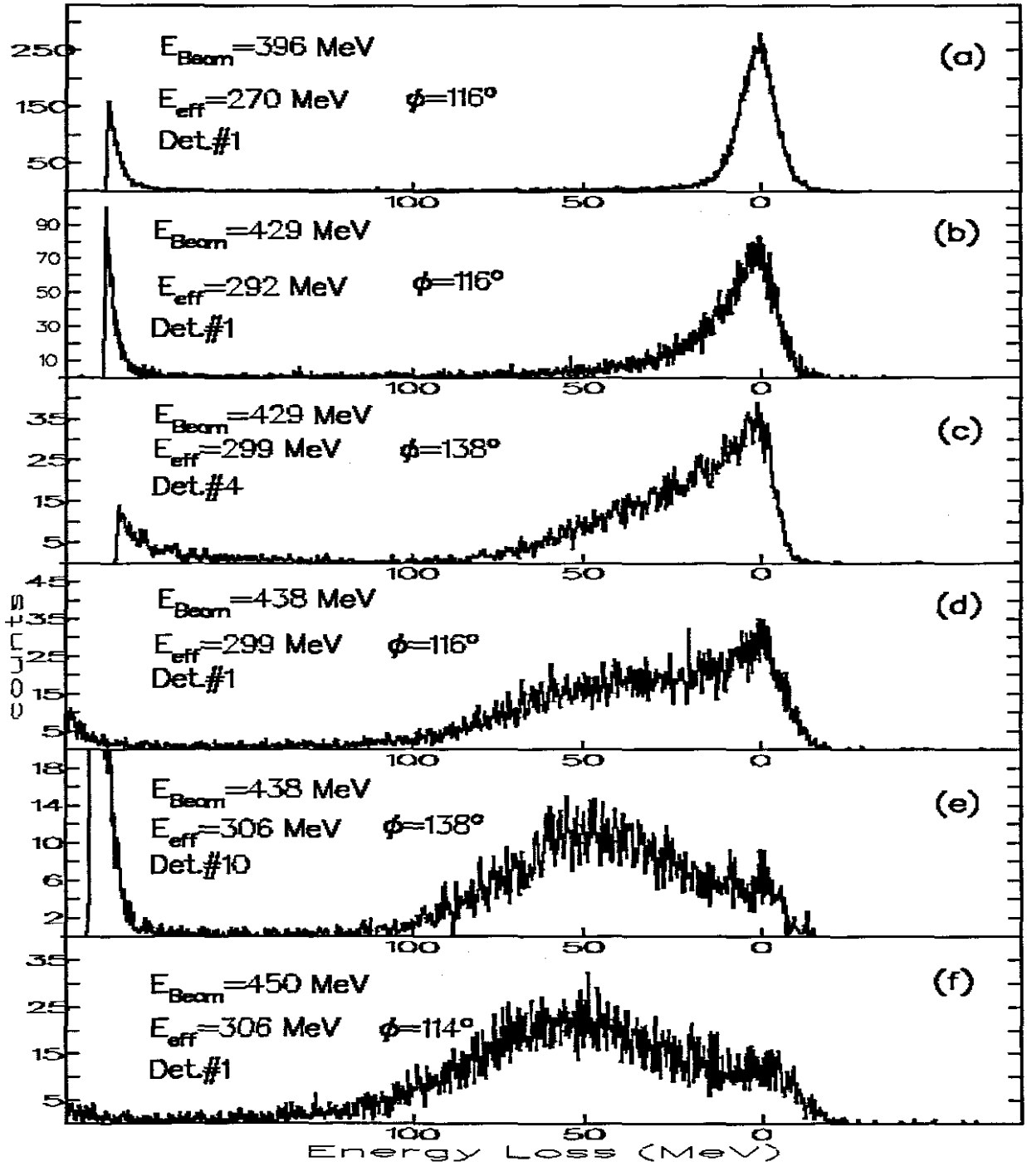

Figure 4-1: *The spectra from photovoltaic cell obtained at different beam energies in the* Laboratory system.

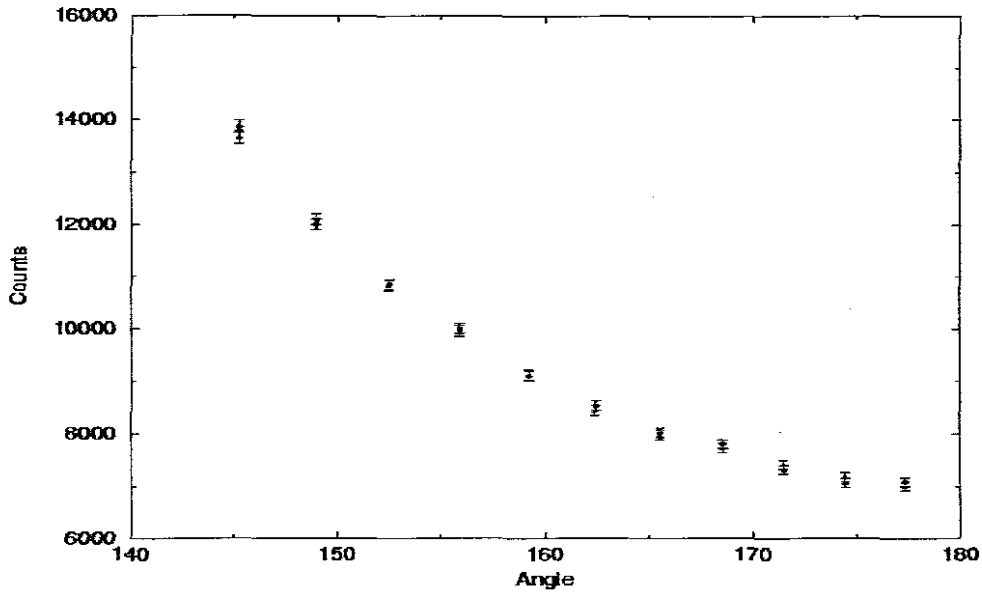

Figure 4-2: The illustration of the count rate of the photovoltaic cells, showing the approximately equal count rate in symmetric photovoltaic cells. The red and black data points are for the bottom and top photovoltaic cells respectively.

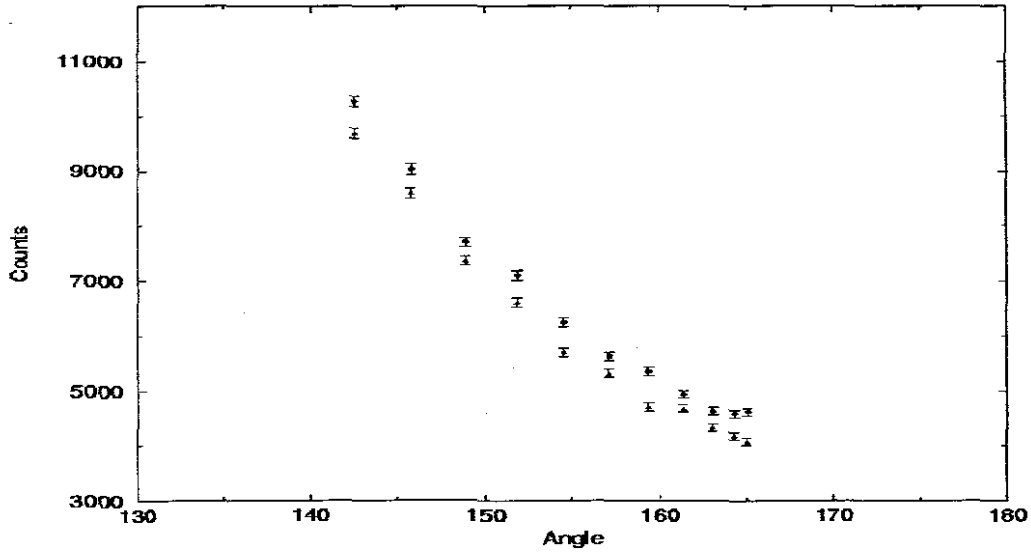

Figure 4-3: The illustration of the count rate of the photovoltaic cells, showing the discrepancy in count rate in the symmetric photovoltaic cells. The red and black data points are for the bottom and top photovoltaic cells respectively.

For every run there was one spectrum obtained from the silicon surface-barrier detector. Three peaks were observed in the spectrum obtained with the silicon detector, which was at a forward angle. Using the program called KINAMAT it was deduced that these peaks correspond to the recoil Carbon, recoil Lead and the scattered Krypton, where the Kr is the peak at highest channel; Pb is the middle and carbon at the lowest channel. The carbon was due to the fact the target used was sputtered with carbon as explained in section 3.3. The Kr peak was used for the normalization, which was the main purpose for placing the silicon monitor detector at 40° in the forward angles.

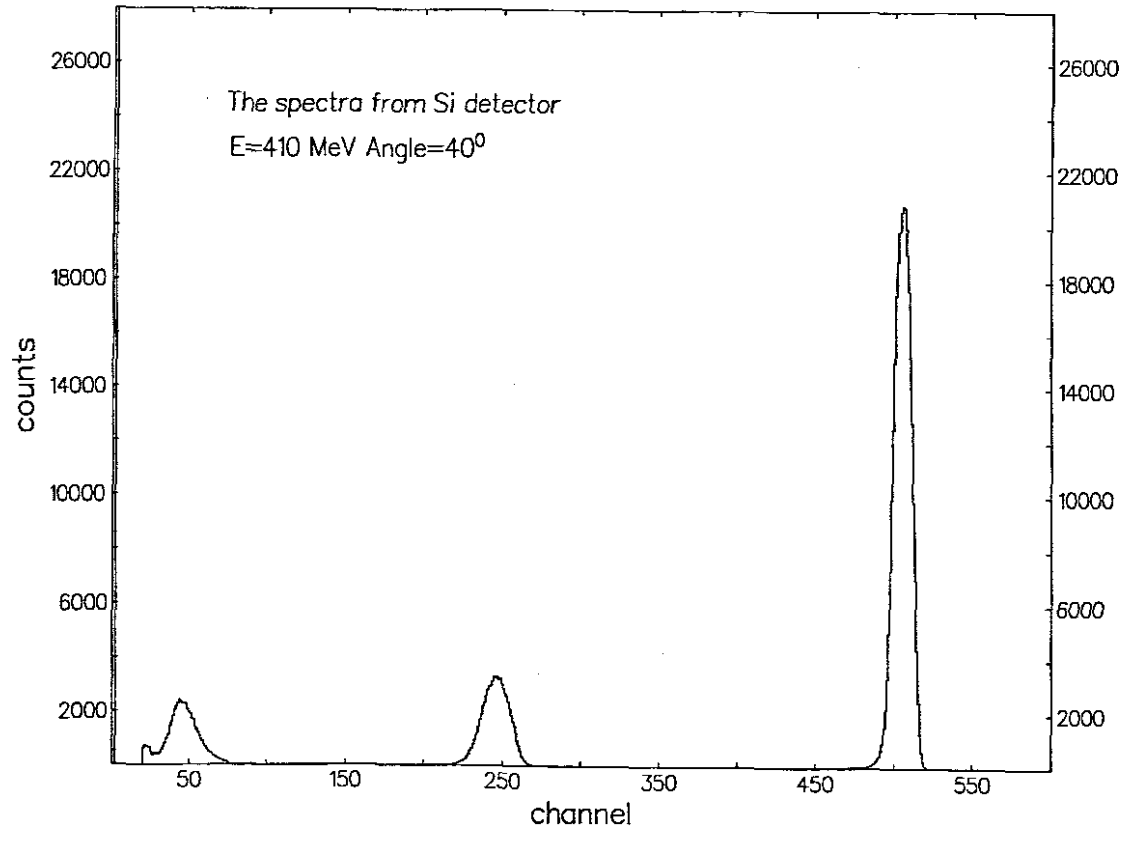

Figure 4-4: The spectrum obtained from the silicon surface barrier detector.

The spectrum from the silicon detector was the same for all energies, except that there was a difference in counts, which was increasing with increasing beam current. A spectrum from the silicon surface barrier is illustrated in figure 4.4.

4.2 ANGULAR DISTRIBUTION

As the monitor detector was placed in the forward angles for the purpose of monitoring the Rutherford scattering, it was then changed to different angles in order to check the scattering variation with angles. Figure 4.5 shows the spectra obtained when the angular distribution was done. It is clear that at large angles the scattering is diminishing, while at very forward angles the peak showed a tail, indicating a contribution from inelastic scattering. Therefore the monitor was placed at 40°, which is very close to the grazing angle, 82.1° for the $^{86}Kr + ^{208}Pb$ system, while still providing a high count rate to obtain enough statistics for normalization purposes.

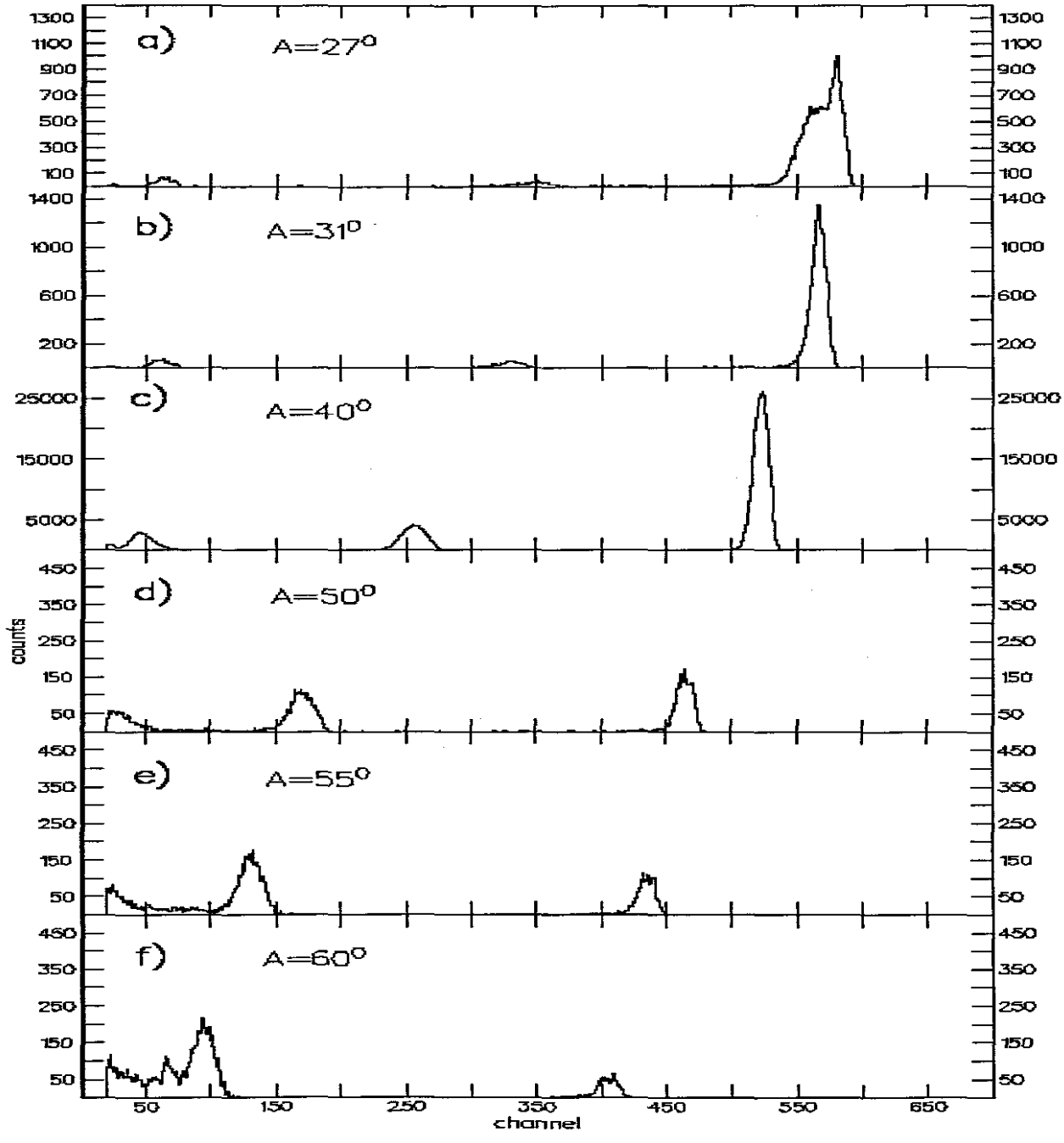

Figure 4-5: The illustration of the unnormalized spectra when the silicon monitor detector was placed in different angles, as indicated in each spectrum at a beam energy of 438 MeV.

4.3 SOLID ANGLE RATIO

There is a difference in the surface area exposed by the detector in the laboratory frame from that in the center-of-mass frame. This discrepancy is corrected by a factor named solid angle ratio. Figure 4.6 illustrates the kinematics of nuclear reactions and scattering. In the figures 4.6 ψ and θ are the lab angles and center-of-mass angle of the scattered particles respectively, and ζ, ϕ are lab angle and center-of-mass angle of the recoil respectively.

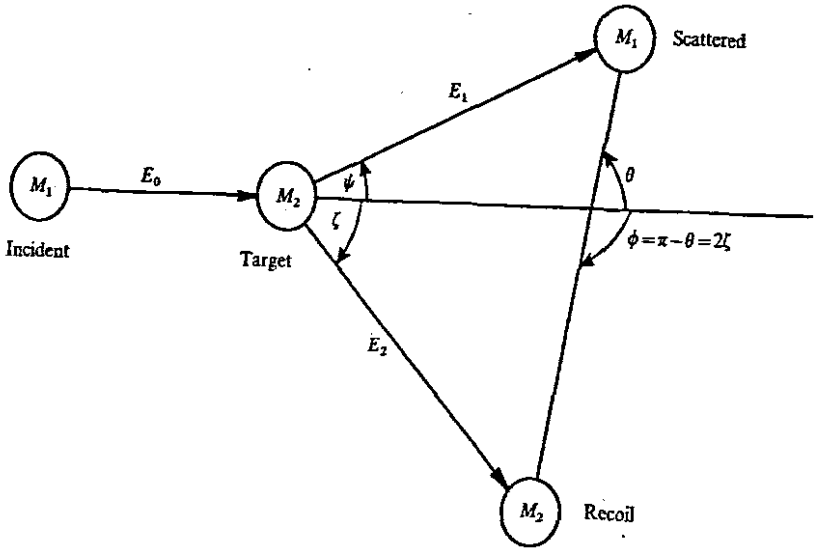

Figure 4-6: illustration of the kinematics of nuclear reactions and scattering, from [Mar68].

From figure 4.6 it can be deduced that the lab angle of the scattered particles is given by

$$\psi = \arctan\left(\frac{m_1/m_2 - \cos\theta}{\sin\theta}\right) \qquad 4.1$$

And the center-of-mass angle of the scattered particle angle is given by

$$\theta = \psi + \arcsin\left(\frac{M_1}{M_2}\sin\psi\right) \qquad 4.2$$

The solid angle ratio of the scattered particles is given by

$$\frac{\sigma(\theta)}{\sigma(\psi)}=\frac{\sin^2(\psi)d\psi}{\sin^2(\theta)d\theta}=\frac{\sin^2(\psi)}{\sin^2(\theta)}\cos(\theta-\psi) \qquad 4.3$$

the lab angle of the recoil is given by

$$\tan\psi=\frac{\sin 2\zeta}{\frac{M_1}{M_2}-\cos 2\zeta} \qquad 4.4$$

hence the solid angle ratio of the recoil is given by

$$\frac{\sigma(\phi)}{\sigma(\zeta)}=\frac{\sin\zeta\, d\zeta}{\sin\phi d\phi}=\frac{1}{4\cos\zeta} \qquad 4.5$$

4.4 EXPERIMENTAL RATIO OF QUASIELASTIC SCATTERING CROSS-SECTION TO RUTHERFORD SCATTERING CROSS SECTION

In order to arrive at the final experimental cross section, the number of counts in every photovoltaic cell and the corresponding analyzed spectra from the silicon monitor had to be converted to a relative cross-section. Since the photovoltaic cells could not identify the particle type, the obtained cross-section is referred to as the quasielastic (the sum of the elastic, inelastic and transfer reaction) cross-section. The quasielastic cross-section is proportional to the number of counts, obtained from the photovoltaic cell:

$$\left(\frac{d\sigma}{d\Omega}\right)_{QE}=\frac{(SAR)_{PV}N_{PV}}{\Delta\Omega_{PV}Qt\epsilon_{PV}} \qquad 4.6$$

Where $\left(\frac{d\sigma}{d\Omega}\right)_{QE}$ is the quasi-elastic cross-section

N_{PV} is the number of counts obtained from each photovoltaic cell spectrum by taking the peak areas.

ϵ_{PV} is the efficiency of the photovoltaic cells

Q is the integrated beam current

t is the thickness of the target

$(SAR)_{PV}$ is the solid angle ratio of the photovoltaic cell

$\Delta\Omega_{PV}$ is the solid angle of the photovoltaic cell.

Likewise for the silicon-surface barrier detector, the cross section is given by

$$\left(\frac{d\sigma}{d\Omega}\right)_R = \frac{(SAR)_{Si} N_{Si}}{\Delta\Omega_{Si} Qt \epsilon_{Si}} \qquad 4.7$$

Since the integrated beam current and the thickness were common to both photovoltaic cells and silicon detector measurements, Qt from equation 4.6 was substituted in equation 4.7 to obtain the quasielastic cross-section. These yield the formula used to calculate the quasi-elastic cross-section:

$$\left(\frac{d\sigma}{d\Omega}\right)_{QE} = \frac{N_{PV}\left(\frac{d\sigma}{d\Omega}\right)_R \Delta\Omega_{Si}\epsilon_{Si}}{N_{Si}\Delta\Omega_{PV}\epsilon_{PV}} \quad mb/sr \qquad 4.8$$

The ratio of the quasielastic cross-section to the Rutherford cross-section, was obtained through the Rutherford formula given by equation 4.9. The theoretical center-of-mass cross-section for the Rutherford scattering is given by [Mar68].

$$\left(\frac{d\sigma}{d\Omega}\right)_R = 1.296\left(\frac{Z_p Z_t}{E_{cm}}\right)^2\left(\frac{M_p + M_t}{M_t}\right)^2 \frac{1}{\sin^4\left(\frac{1}{2}\theta_{cm}\right)} \quad mb/sr \qquad 4.9$$

Where Z_p, Z_t are the charges of the projectile and the target respectively

E_{cm} is the energy in center of mass

M_p, M_t are the masses of the projectile and the target respectively and θ_{cm} is the angle in the center-of-mass.

Subtituting equation 4.9 into equation 4.8 yields

$$\frac{\sigma_{QE}}{\sigma_R} = \frac{N_{PV}\left(1.296\left(\frac{Z_p Z_t}{E_{cm}}\right)^2\left(\frac{M_p+M_t}{M_t}\right)^2 \frac{1}{\sin^4\left(\frac{1}{2}\theta_{cm}\right)}\right)\Delta\Omega_{Si}\epsilon_{si}}{N_{si}\Delta\Omega_{PV}\epsilon_{PV}} \qquad 4.10$$

It was assumed that the efficiencies ϵ_{si} and ϵ_{PV} both equaled unity.

4.5 CORRECTION OF THE MISALIGNMENT

Theoretically the ratio of the quasielastic cross-section to the Rutherford must be equal to one, $\sigma_{QE}/\sigma_R = 1$ at energies well below the barrier, and it should decrease monotonically with increasing energy above the barrier. The lowest energy used in these experiments was 396 MeV, which is about 20 MeV below the Coulomb barrier of $^{86}Kr + ^{208}Pb$.

The resulting σ_{QE}/σ_R is shown in figure 4.7. However, a large spread in the data points is seen for a given energy. The data from the symmetric photovoltaic cells indicated that the beam was not well aligned as is evident from figure 4.3. A misalignment in the vertical direction (y) could be averaged out to first order by summing the counts in photovoltaic cells at complementary angles. In the horizontal (x) direction, the monitor detector was used to correct for misalignment.

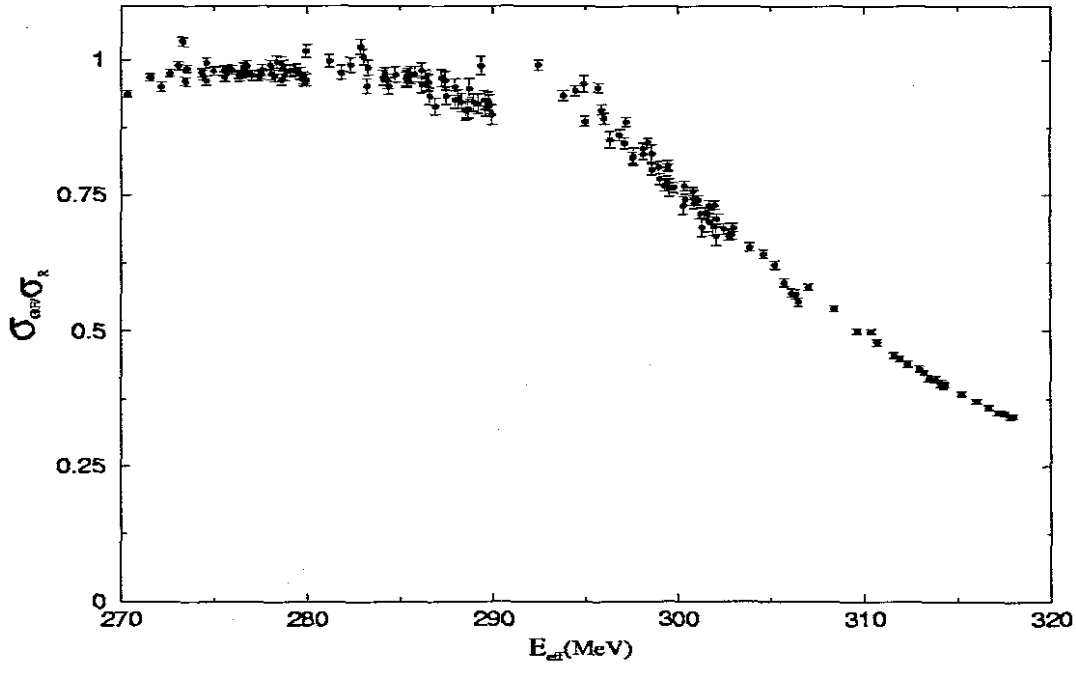

Figure 4-7: The data for the ratio of quasi elastic to the Rutherford scattering of $^{86}Kr + ^{208}Pb$ before the correction of the beam misalignment.

Ideally one would compare the number of scattered Kr particles at $+40^{\circ}$ with those at -40°. However since there was only one monitor detector, the number of counts in the Pb recoil peak was used as a proxy for the number of Kr atoms scattered on the opposite side of the beam. The exact scattering angle of the Kr was calculated from the kinematics. In general this corresponded to about 76°. At these angles the scattering was still Rutherford, as shown in figure 4.5. Therefore, a deviation from the Rutherford Scattering Law would indicate a beam misalignment. If the change in scattering angle due to a misalignment δx in the x-direction is $\delta\theta$, then assuming pure Rutherford scattering, and after correcting the number of counts, N_{Kr} and N_{Pb} with their respective solid angle ratios, we get

$$\frac{(SAR)_{Pb}}{(SAR)_{Kr}}\frac{N_{Pb}}{N_{Kr}} = \frac{\sin^4\left(\frac{\theta_{cm}^{R}+\delta\theta}{2}\right)}{\sin^4\left(\frac{\theta_{cm}^{L}+\delta\theta}{2}\right)} \qquad 4.11$$

Where $(SAR)_{Pb}$ and $(SAR)_{Kr}$ are the solid angle ratio of Pb and Kr respectively

θ_{cm}^{R} is the angle of the Si monitor in the center-of –mass frame

θ_{cm}^{L} is the angle of a Kr atom corresponding to the observed Pb recoil in the center-of -mass frame.

Equation 4.11 can be solved analytically for $\delta\theta$ to give

$$\delta\theta = 2\arctan\left[\frac{K\sin\frac{\theta_{cm}^{L}}{2}-\sin\frac{\theta_{cm}^{R}}{2}}{\cos\frac{\theta_{cm}^{R}}{2}-K\cos\frac{\theta_{cm}^{L}}{2}}\right] \qquad 4.12$$

$$\text{where } K = \left[\frac{(SAR)_{Pb}\,N_{Pb}}{(SAR)_{Kr}\,N_{Kr}}\right]^{\frac{1}{4}} \qquad 4.13$$

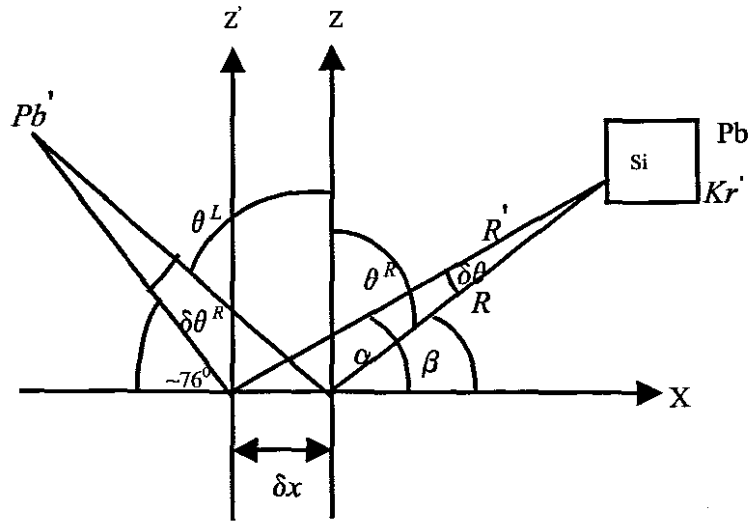

Figure 4-8: Illustration of the position of the detected scattered particle and the recoils. Z is the normal beam direction, aligned with the optical axis of the beam line, while Z' is the actual beam direction, due to misalignment.

Then, using the change in the scattering angle $\delta\theta$, the beam misalignment in the x-direction was determined using equation 4.14, which was extracted from the geometry of figure 4.8:

$$\delta x = R' \cos\alpha - R\cos\beta \qquad 4.14$$

where the parameters R', R, α and β represent the distance from the target to the silicon detector after the deviation, the distance from the target to detector before deviation, angles relative to the beam as shown in figure 4.8. Therefore the new angle of the silicon detector can be determined by the product rule.

$$\cos\theta = \frac{\vec{z'}.\vec{R'}}{|z'||R'|} \qquad 4.15$$

where the position vector are $\vec{z} = (0,0,1)$ and $\vec{R'} = (R\sin\beta - \delta x, -\delta y, R\cos\beta)$

In the y-direction an improved correction was then performed using the photovoltaic cells. Figure 4.9 illustrates the position of a photovoltaic cell with respective to the beam direction. The distance between the z and z' is the deviation in the x-direction. Before any deviation the position vector of the photovoltaic cell was

$$\vec{PV} = \left(P\cos(APV)\cos(Arm-90^0), P\sin(APV), P\cos(APV)\sin(Arm-90^0)\right) \quad 4.16$$

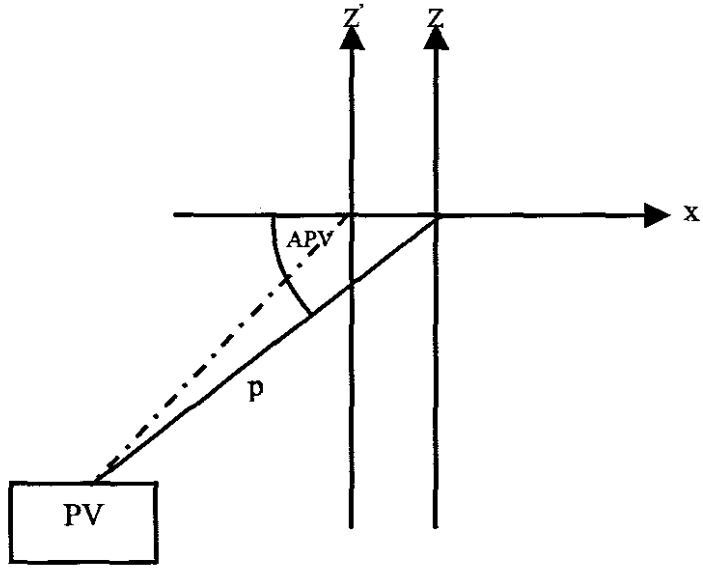

Figure 4-9: Illustration the position photovoltaic cell with respect to the beam direction.

After the deviation δx and δy, the position vector of the photovoltaic cells is given by equation 4.17

$$\vec{PV'} = \left(P\cos(APV)\cos(Arm-90^\circ)+\delta x, P\sin(APV)+\delta y, P\cos(APV)\sin(Arm-90^\circ)\right) \quad 4.17$$

Therefore the angle between the beam direction and the photovoltaic cells can be determined by the dot product of the position vector beam and the photovoltaic cell, hence

$$\cos\Omega = \frac{\vec{z'}\,\vec{PV'}}{|z'||PV'|} \quad 4.18$$

CORRECTION OF THE MISALIGNMENT

The number of counts in symmetric photovoltaic cells was used to determine the deviation in the y-direction. Since the number of count in each photovoltaic cell is given by

$$N^{+} = \frac{d\sigma(\xi_{+})}{d\Omega} Qt\Delta\Omega \qquad 4.19$$

$$N^{-} = \frac{d\sigma(\xi_{-})}{d\Omega} Qt\Delta\Omega \qquad 4.20$$

where N^{+} and N^{-} are the number of counts in the top and bottom photovoltaic cells respectively and $\xi_{\pm}$ are the angles of the photovoltaic cells from the z' axis

$\frac{d\sigma}{d\Omega}$ is the cross section, Q is the integrated beam current, t is the thickness and $\Delta\Omega$ is the solid angle Then

$$\frac{N^{+}}{N^{-}} = \frac{d\sigma(\xi_{+})/d\Omega}{d\sigma(\xi_{-})/d\Omega} \qquad 4.21$$

The cross section $d\sigma(\xi_{\pm})/d\Omega$, as a first approximation, was taken as the measured cross-section, uncorrected for the beam misalignment. Therefore

$$\frac{d\sigma(\xi)}{d\Omega} = f(\xi)\sigma_{R}(\xi) \qquad 4.22$$

Over small intervals, $f(\xi) = m\xi + C$, and equation 4.22 becomes

$$\frac{N^{+}}{N^{-}} = \frac{m\xi_{+} + c}{\sin^{4}\xi_{+}} \cdot \frac{\sin^{4}\xi_{-}}{m\xi_{-} + c}$$

$$\frac{N^{+}(\sin^{4}(\xi_{+} + \delta\theta))(m(\xi_{-} - \delta\theta) + c)}{N^{-}(\sin^{4}(\xi_{-} - \delta\theta))(m((\xi_{+} + \delta\theta) + c)} = 1 \qquad 4.23$$

where m is the gradient, c is the offset and $\delta\theta$ is the change in angle assuming that if the beam shifts up it will move $\delta\theta$ towards every photovoltaic cell which was above and $\delta\theta$ away from all those below the reaction plane.

This equation was solved iteratively for $\delta\theta$ using a computer program from which δy was obtained. The original δx obtained using equation 4.12 assumed $\delta y = 0$. Using the new

(x, y) co-ordinates for z', a new δx, $\delta x'$, was obtained using equation 4.12. However, $\delta x'$ did not differ significantly from δx to warrant further iterations. The resulting σ_{QE}/σ_R is shown in figure 5.1.

4.6 UNCERTAINTY ANALYSIS

4.6.1 Statistical uncertainty

The error bars on the data points in the cross-section represent the statistical error only. According to Knoll [Kno79], if one assumes that the measurement has been drawn from a population whose theoretical distribution function is a Gaussian distribution, one standard deviation on the counts is equal to the square root of the total number of counts, so that range of values $N_i \pm \sigma$ or $N_i \pm \sqrt{N_i}$ will contain the true number counts with 68% probability. A Gaussian distribution was assumed for the peaks so that the error bars represent $\pm\sqrt{N}$, where N is the number of counts. In order to determine the total statistical error if x_i are counts or related variables that are directly measured and for which we know σ_i then the standard deviation for any quantity f derived from these counts or variable can be calculated from

$$\sigma_f^2 = \sum_i \left(\frac{\partial f}{\partial x_i}\right)^2 \sigma_i^2 \qquad 4.24$$

Where $f = f(x_i)$ represents the derived quantities. This equation is well known as the error propagation formula and is applicable to almost every statistical error situation.
From equation 4.24 it can be shown that in the case of both multiplication and division of counts x_i to arrive to a quantity f, then the following expression for determining the errors in f is applicable

$$\sigma_f^2 = f^2 \left(\sum_i \left(\frac{\sigma_{f_i}}{x_i}\right)^2 \right) \qquad 4.25$$

4.6.2 Systematic errors

The contributors to the systematic error are the target thickness, beam energy, electronics dead time and the solid angle ratio of the two types of detectors used, viz silicon and photovoltaic cell. All the uncertainties that are assumed to contribute in the measurement are summarized in tables 4.1 and 4.2.

Due to the poor timing of the phovoltaic detectors, the dead time correction became unreliable and was therefore ignored. Because of the slow counting rate of the detectors however, the dead time was negligible as shown below. The typical counting rate of the photovoltaics was approximately 0.7Hz; for the Si monitor, it was about 140Hz. Each event took 220 μs to process in the acquisition system, giving an average deadtime of

$$\frac{220\mu s}{1s}\ (0.7 \text{ x } 25 + 140) = 0.39\%$$

where 25 is the total number of photovoltaic.

Furthermore, since absolute cross-section were not measured, even this dead time would largely cancel out in producing the ratio σ_{QE}/σ_R .

Energy spread due to:	Energy in MeV
Loss in Pb	0.9
Finite solid angle in photovoltaic cell	0.8
Energy spread of the beam	1.6
Uncertainity in photovoltaic angle/ Beam misalignment	0. 4
Total (added in quadrature)	2.0 MeV

Table 4-1: The uncertainity in the effective energy.

Uncertainity in σ_{QE} *from*	Percent error
Silicon detector angle	0.05
Silicon detector solid angle	0.21
Photovoltaic cell solid angle	0.19
Electronic dead time	0.39
Total (added in quadrature)	0.63

Table 4-2: The uncertainity in the ratio of the quasielastic scattering to the Rutherford.

In this measurement there are two types of systematic errors, the first is the spread in effective energy due energy loss in the target, finite solid angle in the photovoltaic cells, energy spread of the beam and uncertainity in photovoltaic cell angle. The magnitudes of these errors are listed in table 4.1. When added in quadrature a mean spread in energies of 2 MeV is expected.

The second is the cross-section σ_{QE} due to the silicon detector angle, photovoltaic cell solid angle and electronic dead time. The sizes of the errors are listed in table 4.2.

CHAPTER 5 RESULTS AND DISCUSSION

5.1 THE QUASIELASTIC RESULTS FOR ^{86}Kr + ^{208}Pb SYSTEM

The data of the ratio of quasielastic scattering to the Rutherford scattering σ_{QE}/σ_R has been analyzed. Figure 5.1 shows the data for σ_{QE}/σ_R after correcting for beam misalignment. They correspond to centre-of-mass energies between 290 MeV and 320 MeV and scattering angles between 140° and 175°. As mentioned in section 4.2, it is expected that σ_{QE}/σ_R=1 at energies below the barrier. There are a number of reasons which may result in the cross-section not to be equal to the one predicted by the theory; an overestimated of the monitor solid angle, (although this was checked); that the silicon detector was not only measuring the Rutherford cross-section, but there is no evidence of this in the spectra shown in figure 4.4; or that 396 MeV might not be well enough below the barrier, and that Coulomb-nuclear interference is occurring.

The errors shown in figure 5.1 are only statistical, and are about less than one per cent. It has been discussed in section 2.4.3, that the barrier distribution from the quasielastic cross-section can be determined by taking the first derivative. In order to take the derivative of the data it was necessary to smooth the ratio in energy. Before the data was smoothed it was ordered in order of increasing effective energy E_{eff}. Since the total error was about 2 MeV the data were then smoothed over 2 MeV with a Gasusian weighting. The Gaussian weighting is a moving average that produces a continuous function which approximates the average curve that fits the data points. For each data points, the moving average is generated by weighting the neighbouring points with a Gaussian:

$$<\sigma_i> = \frac{\sum_k \sigma_i \exp\left(\frac{-(\exp i - \exp k)^2}{\Delta^2}\right)}{\sum_k \exp\left(\frac{-(\exp i - \exp k)^2}{\Delta^2}\right)} \qquad 5.1$$

where Δ is the width i.e 2 MeV.

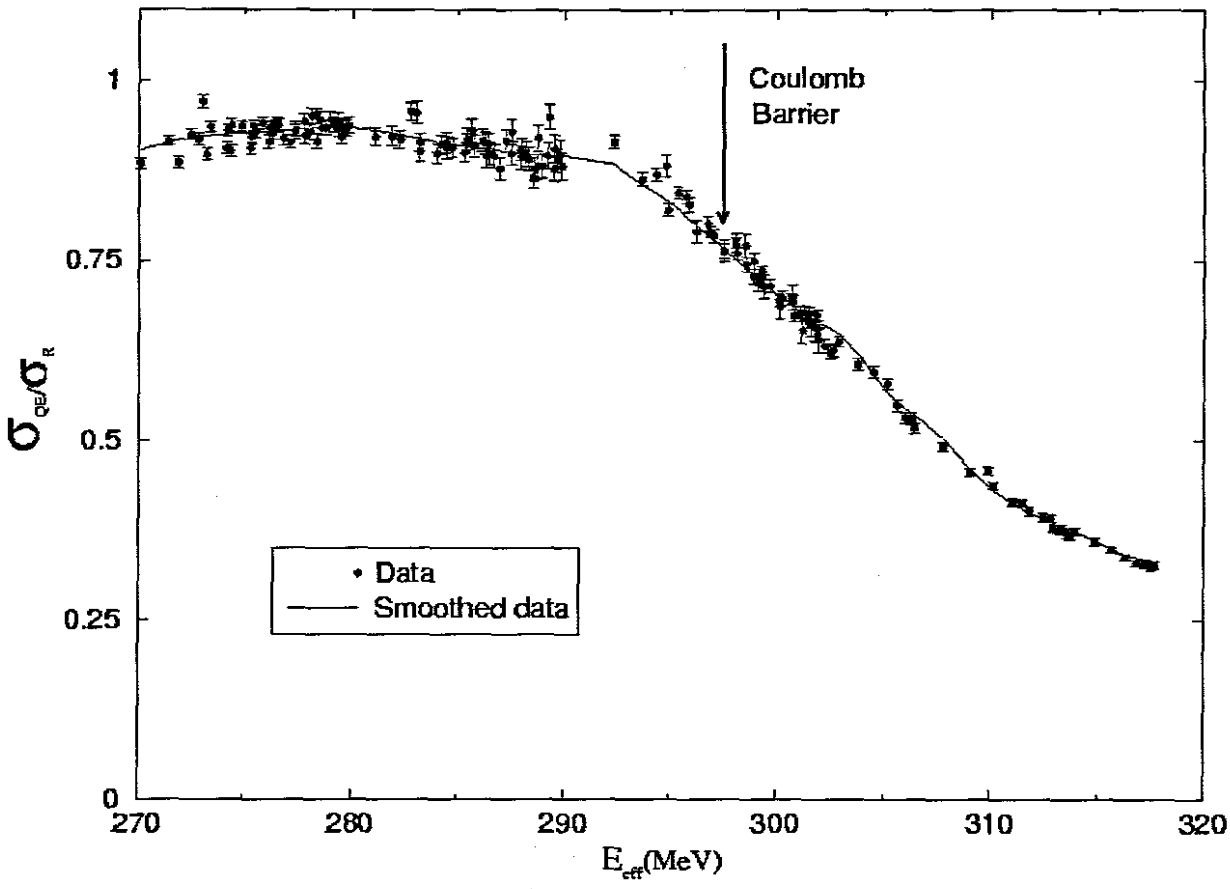

Figure 5-1: The data for the ratio of quasielastic to Rutherford scattering for $^{86}Kr + ^{208}Pb$.

5.2 EXPERIMENTAL BARRIER DISTRIBUTION

The data and the smoothed data are shown together in figure 5.1. The experimental barrier distribution was determined by taking the negative derivative, $D(E_{eff}) = -\frac{d\left(\frac{\sigma_{QE}}{\sigma_R}\right)}{dE_{eff}}$ of the smoothed data, and is shown in figure 5.2.

In order to understand the measured cross-section, the program CCFULL [Hag99] was used to solve the coupled channels equations described in chapter 2. Dr Neil Rowley performed the calculations.

In order to obtain the calculated barrier distribution shown in figure 5.2 the octupole-phonon states (N_{oct}) in the ^{208}Pb target and the quadrupole-phonon states (N_{quad}) in the ^{86}Kr projectile were taken into account.

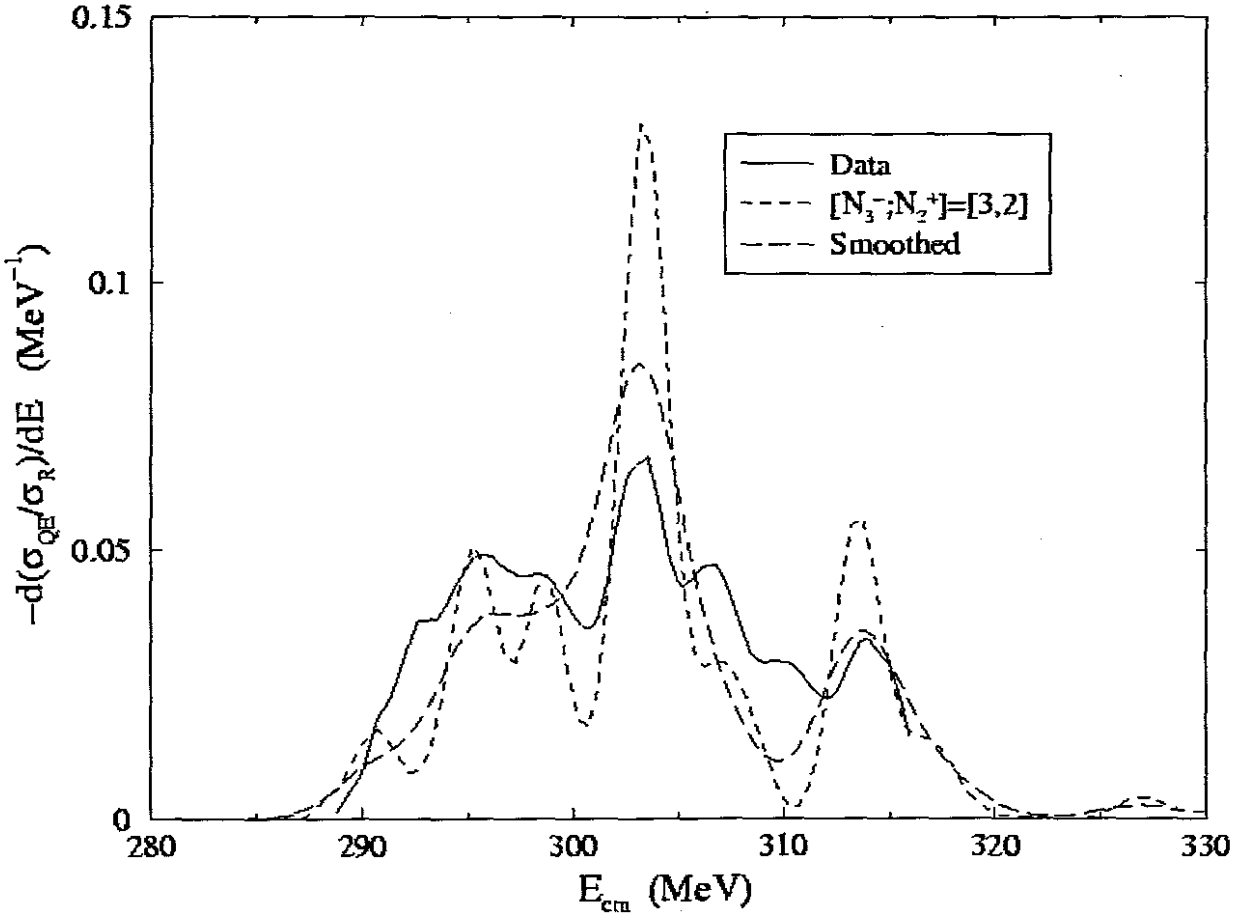

Figure 5-2: Experimental and theoretical barrier distributions for ^{86}Kr + ^{208}Pb. Also shown is the theoretical barrier distribution smoothed over the same energy range (2 MeV) as the data. The theoretical barrier distribution was obtained at $N_3^- = 3$ and $N_2^- = 2$.

It was found that it was necessary to go to $N_{oct} = 3$ and $N_{quad} = 2$ in order to obtain convergence of the results. The 5^- state in the target was found to have a negligible influence.

There is a noticeable similarity in the structure of the barrier distribution obtained from the CCFULL calculation and that from the data. The overall barrier structure from the calculations is still similar to the barriers obtained from data even when it smoothed over the same energy range as the data of figure 5.1.As it has been discussed in section 2.4.2 theoretically the barrier weights should sum to unity, $\int_0^\infty D(B)dB = 1$. However, the sum of the experimental barrier weights was only 0.62. In order to compare the experimental and the theoretical curve, that is to extract the barrier weights that sum to unity, it was necessary to renormalize the experimental barrier distribution by a factor of 1.6, the inverse of the total experimental barrier weights. The total barrier weights of 0.62 imply that the quasielastic cross section which was measured has included other contributions at the highest energy. The value of $\sigma_{QE}/\sigma_R = 0.38$ at that energy is actually not quasielastic scattering but is coming from some other process. Indeed the spectra of the photovoltaic cells in figure 4.1 (b) start to show a contribution at high energies with an average energy loss greatly exceeding the possible energy loss coming from the true quasielastic channels accounted for in the renormalization calculations. The events seen in the photovoltaic cells come from deep-inelastic collisions (DIC). Dr Neil Rowley, in his presentation in St Petersburg, Russia proposed a theoretical method to remove these unwanted events. Using the fact that the deep-inelastic collisions happen after the barrier has been crossed; their cross-section should be proportional to the capture cross-section. In attempt to effectively remove this part of the cross-section the experimental data was manipulated as follows:

The deep-inelastic collision cross-section can be expressed in terms of the capture and the quasielastic cross-section by equation 5.2.

$$\frac{\sigma_{DIC}}{\sigma_R} \propto \frac{\sigma_C}{\sigma_R} = 1 - \frac{\sigma_{QE}}{\sigma_R} \qquad 5.2$$

Assuming k to be the proportionality constant, equation 5.2 can be written as:

$$\frac{\sigma_{DIC}}{\sigma_R} = k\left(1 - \frac{\sigma_{QE}}{\sigma_R}\right) \qquad 5.3$$

The acquired experimental cross-section is given by

$$\frac{\sigma_A}{\sigma_R} = \frac{\sigma_{DIC} + \sigma_{QE}}{\sigma_R} \qquad 5.4$$

It therefore follows that the quasielastic cross-section can be obtained by

$$\frac{\sigma_{QE}}{\sigma_R} = \frac{\sigma_A}{\sigma_R} - \frac{\sigma_{DIC}}{\sigma_R} \qquad 5.5$$

substituting the deep-inelastic cross-section by equation 5.3 in equation 5.5 gives

$$\frac{\sigma_{QE}}{\sigma_R} = \frac{\sigma_A}{\sigma_R} - k\left(1 - \frac{\sigma_{QE}}{\sigma_R}\right) \qquad 5.6$$

which simplifies to

$$\frac{\sigma_{QE}}{\sigma_R} = \frac{\sigma_A/\sigma_R - k}{1-k} \qquad 5.7$$

Taking k to be the lowest acquired cross-section at higher energies, $k = 0.38$ equation 5.7 becomes

$$\frac{\sigma_{QE}}{\sigma_R} = \frac{\sigma_A/\sigma_R - 0.38}{0.62} \qquad 5.8$$

In this way the pure quasielastic cross-section has been extracted from the acquired cross-section which was contaminated with the deep-inelastic collision cross-section. This yield the quasielastic scattering cross-section shown in figure 5.3.

The width of the fall-off region of the true quasielastic scattering is then seen to be rather well reproduced by the CCFULL multi-phonon-coupling calculations, and possibly even some of the detailed structures seen in figure 5.2. This interpretation is supported by the large-angle photovoltaic cell which show the quasi-elastic peak, evident at low energies figure 4.1 (e), being swamped by the deep-inelastic contribution at the highest energies.

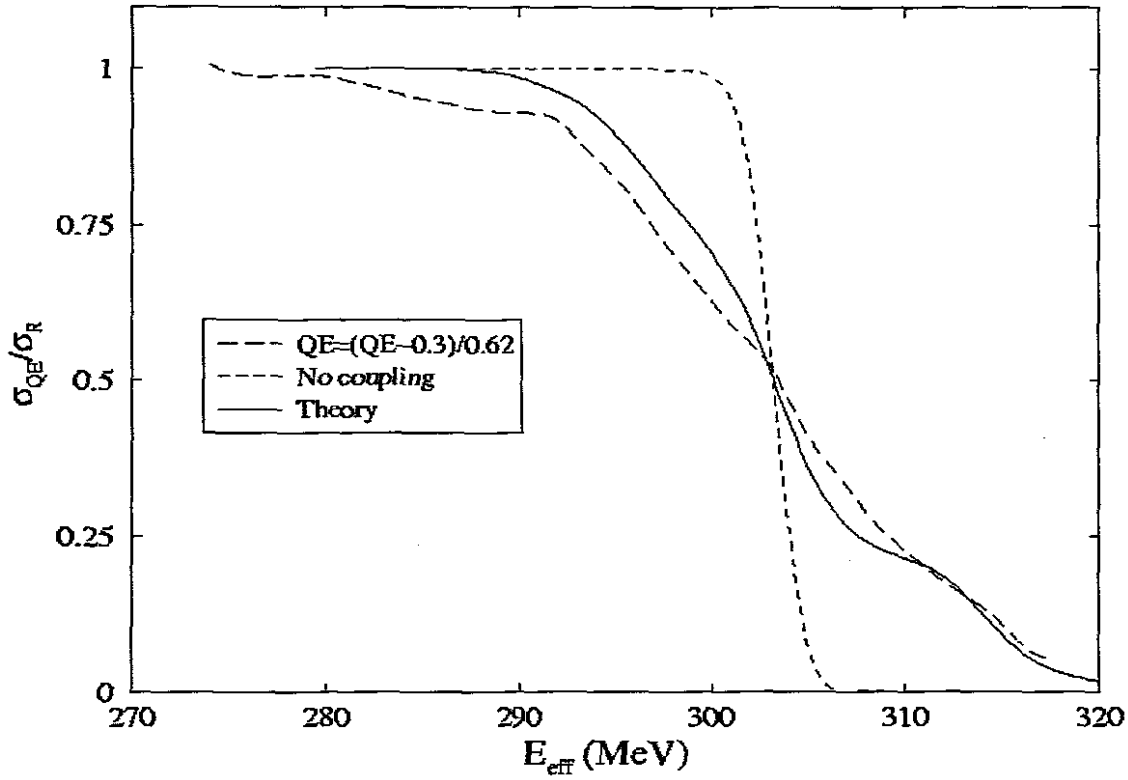

Figure 5-3: Comparison of the theoretical quasielastic cross section with the proposed theoretical removal of DIC events and the uncoupled calculation.

5.2.1 Extracting pure quasielastic

Knowing that the events recorded on the photovoltaic cells at the higher energies are mostly from deep inelastic reactions, an attempt was made to separate the inelastic events from the DI events in the photovoltaic cells spectra. First a Gaussian was fitted to the pure elastic scattering events at energies below the barrier (E_{Lab}=396MeV and E_{Lab}=410 MeV) for each photovoltaic cell. These determined an energy calibration, and also the width of the quasielastic peak. Then quasielastic events at higher energies (E_{Lab}=429 MeV, E_{Lab}=438 MeV, E_{Lab}=450 MeV) were obtained by fitting a Gaussian with position fixed at that predicted by the energy calibration from the pure elastically scattered events, at low energies. The width of the Gaussian was also fixed to the width found at energies below the barrier. Using this method the ratio of the quasielastic to the Rutherford was

obtained as shown in figure 5.4. This result is in excellent agreement with the cross-section predicted assuming that the deep inelastic cross-section is proportional to the capture cross-section.

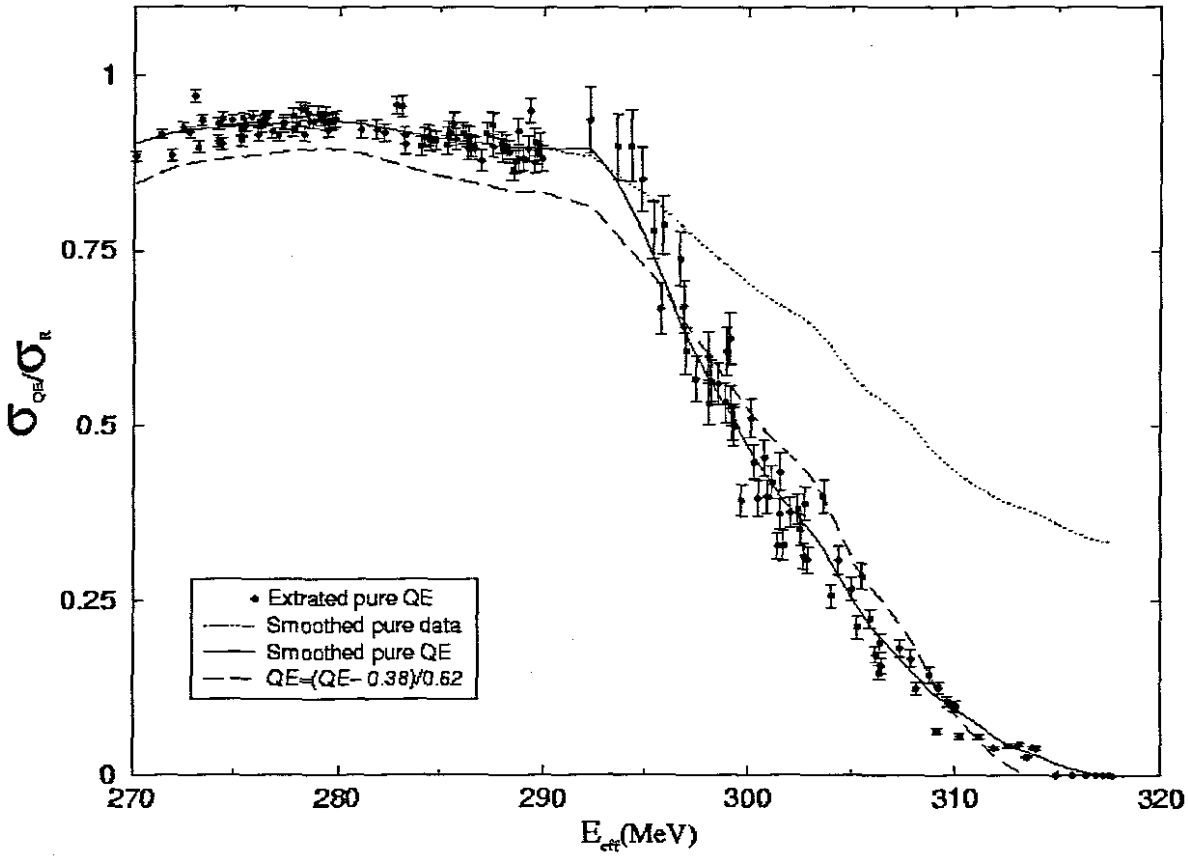

Figure 5-4: The figure compares the cross-section ratio obtained when using different methods of extracting the deep-inelastic collision events from quasielastic events.

CHAPTER 6 SUMMARY AND CONCLUSION

The work presented in this thesis is based on a measurement of fusion barrier distribution performed at iThemba LABS, South Africa. This is one of the attempts to obtain the capture cross section by exploiting unitarity, that is by measuring the flux reflected from the barrier at large angles. This is the first time that the barrier distribution has been measured in this way for such a complicated and heavy system. It was found, however that there are complications arising from events in the detectors coming from deep-inelastic collisions. An approximate experimental method was proposed to unfold these deep-inelastic collision events. These results strongly imply that deep inelastic scattering can be understood as a process that occurs after the barrier has been crossed, and that the remaining quasielastic channel can then be well described by coupled channels calculations.

REFERENCES

[Ada04] G.G. Adamian et al., Phys. Rev C **69** (2004) 011601

[And88] M.V. Andres, N. Rowley and M.A. Nagarajan, Nucl. Phys. **A 481** (1988) 600.

[Arm85] P. Armbruster, Ann, Rev. Nucl. Part. Sci.**35**, 135 (1985).

[Bac85] B.B. Back, Phys. Rev. C **31** (1985) 2104.

[Bal86] A.B. Balantekin and P.E. Reimer, Phys. Rev. C **33** (1986) 379.

[Bas77] R. Bass, Phys Rev. Lett. **39** (1977) 265.

[Bas80] Reiner Bass, Nuclear Reactions with Heavy Ions, Berlin Heidelberg New York 1980, p289.

[Bec88] M. Beckerman, Rep. Prog. Phys.**51** (1988) 1047.

[Blo86] J.P. Bolcki, H. Feldemeir, W.J. Swiatecki, Nucl. Phys. **A 459** (1986) 145.

[Boh39] N. Bohr, J.A Wheeler, Phys. ReV. **56** (1939) 426.

[Bra00] P.D. Bradley, PhD Thesis, University of Wollongong, unpublished, 2000.

[Bud81] A. Budzanowski, Dynamics of Heavy-Ion Collisions, Conf. Proc., ed Yogoslavia (1981).

[Das83] C.H. Dasso, S. Landowne and A. Winter, Nucl. Phys. **A 405** (1983); A **407** (1983) 221.

[Das98a] M. Dasgupta, D.J. Hinde, N. Rowley and A.M Stefanni, Ann. Rev. Nucl. Part. Sci. **48** (1998) 401-461.

[Den00a] V. Yu Denisov, Eur. Phys. J. A **7**, 87-99 (2000).

[Den00b] V.Yu. Denisov and Hofmann, Phys. Rev.C61 (2000) 034606.

[Des90] A. De Shalit and H. Feshbach. Theoretical Nuclear Physics, Vol.1, Wiley, New York (1990).

[Dut87] Z. B. du Toit, P. J. Celliers, L. M. M. Roels, E .P. Conard, J .J. Burger, Proc. 11th int. Conf. On Cycloctrons and their Applications, Ionics, Tokyo, 109 (1987).

[Ele94] F. Elem, A.T Chastits, Yadra **25**, 295-311 (1994).

[Fes92] H. Feshbach, Theoretical Nuclear Physics, Vol.2, Wiley, New York (1992).

REFERENCES

[Fro65] N. Froman, P.O. Froman, JWKB aprroximation, North-Holland, Amsterdam (1965).

[Gle75] N.K. Glendenning., Rev. Mod. Phys. **47**, 659 (1975).

[Hag04] K. Hagino and N. Rowley, Phys. Rev. C **69**, 054610 (2004).

[Hag99] K. Hagino, N. Rowley, A.T. Kruppa, Comput. Phys. Commun. 123 (1999) 143.

[Hil53] D.L. Hill, J.A. Wheeler, Phys. Rev. **89** (1953) 1102.

[Hil92] D. Hilscher, H. Rosser, Ann. Phys. **17** (1992) 471.

[Hin95] D.J. Hinde et al., Nucl. Phys. **A 592** (1995) 271.

[Hod71] P.E. Hodgson, Nuclear Reactions and Nuclear Structure, Carendon press, (1971)

[Hof00] S. Hofmann and G. Münzenberg, Rev.Mod.Phys. **72**, 733 (200).

[Hof01] S. Hofmann et al., Eur. Phys.J. A10 (2001) 014303.

[Hof97] S. Hofmann et al., Nucl. Phys. **A616** (1997) 370c.

[Hui81] J.R. Huizenga, Dynamics of Heavy-Ion Collisions, Conf. Proc.,ed Yogoslavia (1981).

[Ike00] H. Ikezoe, Ken-Ichiro Satou, Sinichi Mitsuoka, Katsuhisa Nishio,Kaoru Tsuruta, Sun-Chang Jeong, and Cheng-Jiang Lin, Phys. Rev C **62** (2000), 014602

[Jor86] J. Jortner and B. Pullman. The Jerusalem Symposia on Quantum Chemistry and Biochemistry, Tunneling. Eds. Volume 19. D. Reidel Publishing Company, Dordrecht, Holland (1986).

[Kem36] E.C. Kemble, Phys. Rev. 48 (1936) 546.

[Kno79] J. Knoll Phys. Rev. C **20**, 773, (1979).

[Kra88] K.S. Krane, Introductory Nuclear Physics, Wiley, Canada (1988) 242.

[Kru93] A.T. Kruppa et al., Nucl. Phys. **A560** (1993) 845.

[Lef76] M. Lefort Rep. Prog. Phys. (1976) 39129-173.

[Lei82] J.R. Leigh et al., Phys. Rev. Lett. **48** (1982) 527.

[Lei95] J.R. Leigh, et al. Phys. Rev C **52**:3151 (1995).

[Lem93] R.C. Lemmon, J.R Leigh, J.X Wei, C.R. Morton, D.J. Hinde, J.O. Newton, J.C. Mein, M. Dasgupta and N. Rowley, Phys. Lett. B **316** (1993) 32.

[Lin84] R. Lindsay, N. Rowley, J. Phys. G: Nucl. Part. Phys. **10** (1984) 805

[Loe87] W.R. Leo, Techniques for Nuclear and Particle Physcs Experiments, published in Springer-Verlag Berlin Heidelberg New York London Paris Tokyo (1987).

[Mar68] J.B. Marin/ F.C. Young, Nuclear Reaction Analysis, Published by Northern Holland-Publishing Company, 1968.

[Möl94] P. Möller, J.R. Nix, J.Phys.G: Nucl. P.Phys.**20** (1994) 1681.

[Mos69] U. Mosel and W.Greiner, Z. Phys.**A222** (1969) 261.

[Mos80] U. Mosel, In Heavy Ion Physics, ed. R. Boc, Vol.2 (North Holland, Amsterdam, 1980) p.275.

[Mos81] U. Mosel, Proceedings of the 3rd Adriatc Europhysics Study Comference on the Dynamis of Heavy-Ion Collisions Hvar, Croatia, Yugoslavia 25-30,1981 p4.

[Pia02] E. Piasecki et al., Phys. Rev. C **65** (2002).

[Pil96] J. V. Pilcher The NAC MBD to VME Conversion Guide, National Accelerator Center (1996) (unpublished).

[Pla84] F. Plasil et al., Phys. Rev. C **29** (1984) 1145.

[Pro79] F.W. Prosser, Phys. Rev. C **20** (1979) 1305.

[Qui93] A.B. Quint, W. Reisdorf, K.H. Schmidt, P.Armbruster, F.P. Hessberger, S. Hofmann, J. Keller, G. Müzenberg, H. Stelzer, H.G Clerc, W. Morawek, and C.C Sahm, Z. Phys. A **346** (1993), 119.

[Rho84] M.J. Rhoades-Brown, P. Braun-Munzinger, Phys. Lett. **B 136** (1984) 19.

[Ria00] RIA, The Rare sotope Accelerator Project, www.phy.anl.gov/ria (2000).

[Row90] N. Rowley Proceedings of Workshop on Heavy Ion Collisions at Energies Near the Coulomb barrier held at Daresbury Laboratory, England, July 1990, p177-190.

[Row91] N.Rowley, G.R. Satchler, and P.H. Stleson, Phys. Lett. **B 254** (1991) 25.

REFERENCES

[Sch68] Leonard I. Schiff, Quantum Mechanics 3rd edition, Kogakusha Company, LTD, Tokyo, 1968, p308.

[Sch84] W.U. Schroder and J.R. Huizenga, Treatise on Heavy-ion Science, Vol.2 ed. D.A. Bromley (Plenum, New York, London, 1984).

[Sch91a] K.H. Schmidt and W. Morawek, Rep. Prog. Phys. **54** (1991), 949.

[Sch91b] R.Schmidt, G. Seifert and H.O. Lutz, Phys. Lett. **A158** (1991) 231-236.

[Smi83] U. Smilansky, P.M. Jacobs, Phys. Lett. B127 (1983) 313

[Smo94] R. Smolanczuk et al., Phys. Rev. C **52** (1995) 8171.

[Sob94] A. Sobiczewski, Phys. Particles Nucl. **25** (1994) 295.

[Ste88] P.H. Stelson, Phys. Lett. **B205** (1988) 190.

[Ste94] A.M. Stefanini, Heavy Ion Fusion, Conf. Proc., ed, World Scientific, Singapore (1994).

[Sto78] Stokstad RG, et al., Phys.Rev. Lett. **41**:465 (1978).

[Sto80] R. G. Stokstad, Phys. Rev. C 21, 2427–2435 (1980).

[Swi81] W.J Swiatecki, Phys. Scripta **24** (1981) 113.

[Tam65] T. Tamura, Rev. Mod. Phys. **37** (1965) 679.

[Ter01] M. Terasawa et al., APJ **562**, 470 (2001).

[Tho59] T.D. Thomas, Phys. Rev. **116** (1959) 703.

[Tim04] H. Timmers et al., Nucl. Phys. **A584** (1995) 190-204.

[Tim95] H.Timmers, J. R. Leigh, M. Dasgupta, D.J Hinde, R.C. Lemmon, J.C Mein, C.R Morton, J.O. Newton, and N Rowley, Nucl. Phys. **A584**, 190 (1995).

[Tim96] H. Timmers PhD Thesis, The Australian National University, Canberra, 1996.

[Wei37] V. Weisskopf, Phys. ReV. **56** (1937) 295.

[Won73] S. Wong.et al., Nucl. Phys. **A564** (1973) 011653.

[www1] http://www.atomicarchive.com/Fission/Fission1.shtml.

[Yod94] N.R. Yoder IUCF VME Data Acquisition system User Information, Indiana University Cyclotron Facility (1994) (unpublished).

[Zag04] V.I. Zagrebaev, Prog. Theor. Phys. (Kyoto), Suppl.**154** (2004) 122.